Atmos. Chem. Phys., 26, 8255–8274, 2026
https://doi.org/10.5194/acp-26-8255-2026

Atmospheric Chemistry and Physics
Open Access
EGU

Research article

OH-initiated aqueous photooxidation of smoke extracts from maize straw and coal combustion: optical properties and molecular composition

Zhaolian Ye[1], Dandan Hu[1], Qiuyan Chen[1], Xiangpeng Huang[1], and Xinlei Ge[2]

[1]School of Resources and Environmental Engineering, Jiangsu University of Technology, Changzhou 213001, China
[2]School of Energy and Environment, Southeast University, Nanjing 211189, China

Correspondence: Zhaolian Ye (bess_ye@jsut.edu.cn) and Xinlei Ge (xinlei@seu.edu.cn)

Received: 4 January 2026 – Discussion started: 23 February 2026
Revised: 5 May 2026 – Accepted: 10 May 2026 – Published: 12 June 2026

Abstract. Aqueous-phase •OH photodegradation of coal- and maize-derived smoke extracts was investigated to elucidate their optical and molecular transformations. Parallel factor analysis of excitation-emission matrix fluorescence spectra identified one humic-like and two protein-like substances. FT-ICR MS revealed that CHO (74.5 % for maize, 58.9 % for coal) and CHON (24.1 % for maize, 11.8 % for coal) compounds dominated both smoke extracts, whereas sulfur-containing species were more abundant in coal smoke (29.4 %) than in maize (1.4 %). The aqueous •OH photooxidation enhanced molecular saturation and reduced aromaticity, reflected by lower double bond equivalent and aromaticity index values. The abundance of lignin-like compounds decreased, whereas lipid- and aliphatic-like fractions increased, suggesting a transformation of aromatic species into more saturated products, which correspondingly reduced light absorption and overall fluorescence intensity. Distinct photodegradation pathways were observed for coal and maize extracts based on changes in resistant, degraded, and newly formed molecules. Reactive species contributed to WSOC degradation in the order •OH $>$ $^3C^*$ $>$ $^1O_2$, with contributions of 86.4 %, 12.8 %, and 0.8 % for coal extracts, and 80.9 %, 16.0 %, and 3.1 % for maize extracts, respectively. Increased oxalic acids, CHO_2^+ fragments, and declining pH values during the first 5 h indicated substantial formation of carboxylic acids. Measurements from aerosol mass spectrometry showed increasing oxidation indicators during this early stage, confirming enhanced oxidation of aqueous secondary organic aerosol. Oxidative potential, assessed by dithiothreitol consumption, initially increased and then declined, while its normalization by water-soluble organic carbon increased, likely due to the formation of nitrogen-containing compounds in coal smoke and reactive quinones in maize smoke, respectively. Overall, this study improves understanding of aqueous-phase photochemical processing of smoke-derived water-soluble organic matter and supports more accurate representation of these processes in atmospheric models, contributing to better assessments of smoke aging impacts on air quality and climate.

1 Introduction

The atmospheric aqueous phase contains a variety of oxidants, such as hydrogen radical (•OH), peroxyl radicals, singlet oxygen ($^1O_2$), and excited triplet states of organic compounds ($^3C^*$), which can trigger aqueous-phase oxidation reaction. Aqueous-phase process has been recognized as a significant source of secondary organic aerosol (SOA) and key contributors to light-absorbing compounds, thereby influencing radiative forcing and air quality (Arciva et al., 2024; Go et al., 2023). Extensive studies have investigated the chemical composition, light-absorption properties, and SOA mass yield from single-component model compounds (Arciva et al., 2022; Li et al., 2022). Recently, increasing attention has been toward the aqueous photoaging of complex mixtures, including laboratory-generated SOA or multicom-

ponent systems (Gerritz et al., 2024; Go et al., 2024). Moreover, studies on aqueous aging of water-soluble organic matter (WSOM) derived from actual smoke particle or $PM_{2.5}$ extracts provide valuable insights into aqueous-phase processing under more realistic atmospheric conditions (Fan et al., 2018; Hems et al., 2020; Wong et al., 2017). Organic matter (OM) within smoke particles, which accounts for up to 60 %–90 % of total mass, is a complex mixture of aromatic and aliphatic compounds with diverse functional groups. The chemical complexity of these precursors poses challenges for comprehensive product characterization and mechanistic studies. Molecular-level compositional data are therefore crucial for improving our understanding of the role of smoke-derived OM in atmospheric aqueous-phase chemistry. High-resolution mass spectrometry (MS) techniques with soft ionization methods, such as Fourier transform ion cyclotron resonance mass spectrometry (FT-ICR MS), enable detailed molecular characterization in complex mixtures and have been widely applied in aerosol studies (Cao et al., 2025; Wang et al., 2017).

To date, only a few studies (Leresche et al., 2021; Lei et al., 2024) have examined photochemical aging characteristics of aqueous extracts of smoke particles or atmospheric fine particular matter, most of which have appeared only recently. Notably, few investigations have compared the molecular and optical changes during aqueous-phase oxidation of smoke extracts from different fuel sources. Cao et al. (2025) compared molecular-level composition and fluorophore changes of extracted WSOM, but their study did not consider the distinct contributions of various reactive oxygen species (ROS) to the oxidation process. Additionally, the wavelength of the light source can significantly influence the photochemical reactivity of organic compounds. For instance, syringaldehyde was found to inhibit the degradation of vanillyl alcohol under UV-B irradiation due to light-absorbing competition, whereas it promoted the degradation of vanillyl alcohol under UV-A irradiation via the photosensitization effect of syringaldehyde (Li et al., 2024a).

To elucidate the reaction mechanism involved in aqueous-phase photooxidation, it is crucial to understand the formation, transformation, and roles of ROS during photolysis. Biomass burning smoke – such as that produced from agricultural crop residues – contains a variety of potential organic photosensitizers bearing with carbonyl groups and conjugated double bonds, which can absorb sunlight and generate ROS (e.g., $HO_2/O_2^{-\bullet}$, $^1O_2$, •OH), thereby enhancing atmospheric oxidative capacity. However, direct quantification of ROS remains challenging (Gerritz et al., 2024; Leresche et al., 2021; Manfrin et al., 2019). For instance, Gerritz et al. (2024) investigated the photolytic formation of ROS in aqueous extracts of laboratory-generated SOA using an in situ UV-vis irradiation system coupled with electron paramagnetic resonance (EPR) spectroscopy and identified organic peroxides and carbonyls as major ROS precursors. Manfrin et al. (2019) reported the $^1O_2$ formation from photosensitized reactions mediated by aromatic SOA, although free radicals were not directly measured. Due to the chemical complexity of smoke-derived WSOM and the analytical difficulty in quantifying ROS, the underlying reaction mechanisms remain poorly understand.

Further investigation into the aqueous photoaging of WSOM from different combustion sources is crucial to understanding the underlying mechanisms driving chemical transformation and light absorption. Comparative studies of maize- and coal-derived WSOM under simulated sunlight can reveal how source-dependent compositions influence photo-reactivity and light-absorbing compounds formation. This study compares the optical, molecular evolution and oxidative potential of maize (a representative agricultural residue) and coal smoke extracts during OH-induced photooxidation. WSOM from both smoke types were analyzed using UV-vis spectrometer, excitation-emission matrix (EEM) fluorescence, and FT-ICR MS to identify similarities and differences in photoaging behavior. High-resolution time-of-flight aerosol mass spectrometers (HR-AMS) were used to characterize the bulk chemical composition of low-volatility organics (denoted as aqSOA) over photoreaction. Our findings will provide insights into the chemical evolution and environmental impacts of smoke-derived organic matter.

2 Materials and Methods

2.1 Chemicals and solutions

The following reagents were purchased from the Sigma-Aldrich (dithiothreitol, > 99 %; 5,5'-dithiobis (2-nitrobenzoic acid), > 99 %; benzoic acid, > 99 %; syringol, > 99 %; furfuryl alcohol, > 99 %). Methanol (≥ 99 %), acetonitrile (≥ 99 %), Na_2CO_3 (≥ 99 %) and $NaHCO_3$ (≥ 99 %) were purchased from Acros Chemicals. Sulfuric acid (≥ 99 %) was obtained from Sinopharm. $(NH_4)_2SO_4$ (GR), H_2O_2 (29 %–32 %) and KOH (≥ 99 %) were supplied by Aladdin and Alfa Aesar, respectively. 2,2,6,6-Tetramethylpiperidine (≥ 98 %) and 5,5-dimethyl-1-pyrroline N-oxide (≥ 97 %) were purchased from Anpel Laboratory Technologies (Shanghai) Co., Ltd.

All chemicals were used as received without further purification. All solutions were prepared with ultrapure water (resistivity ≥ 18.2 MΩ cm) produced by a Milli-Q purification system.

2.2 Sample collection and experiment preparation

Coal and maize straw were collected from Lingwu (Ningxia) and Shangqiu (Henan Province), respectively, and combusted in a self-built stove designed to simulate domestic fuel burning conditions. Smoke particle collection followed the procedures described in our previous study (Ye et al., 2025). Briefly, the stove was connected to a stainless steel dilution tunnel and residence chamber. Smoke particles emitted

from maize straw and coal combustion were collected on pre-baked quartz fiber filters (20.3 × 25.4 cm, Whatman) using two samplers equipped with cyclone with a 2.5 µm aerodynamic cutoff.

One quarter of each filter was cut into strips and placed in extraction bottles. The samples were ultrasonically extracted three times with 30 mL Milli-Q water. The combined extracts were filtered through a 0.45 µm PTFE membrane and subsequently diluted to approximately 15 mg C L^{-1} for photoaging experiment based on suggested TOC level (0.5–1.4 mmol C L^{-1}) by Cook et al. (2017) for cloud water. Photochemical reactions were performed in a Rayonet RPR-200 photoreactor equipped with 14 lamps, following the procedure described in our previous study (Ye et al., 2025). The irradiance intensity on the solution surface was 2.4 mW cm^{-2} in the wavelength region of 290–400 nm (centered at 313 nm), as measured by a radiometer (Photoelectric Instrument Factory of Everfine Corporation, Hangzhou, China). The intensity is slight lower than natural sunlight levels (6.16 mW cm^{-2}) measured at noon during winter at Jiangsu University of Technology (Wang et al., 2025). Before photooxidation, 10 mM H_2O_2 was added to the reaction solution to generate •OH with certain concentration, consistent with previous study (Arciva et al., 2022; Cao et al., 2025).

2.3 Chemical analysis

Water-soluble organic carbon (WSOC) concentrations were determined using a total organic carbon (TOC) analyzer (TOC-L CPH, Shimadzu, Japan). Metal element concentrations (Fe and Cu) were quantified by inductively coupled plasma-mass spectrometry (ICP-MS, Agilent 7800). Eight water soluble inorganic ions (Na^+, Cl^-, SO_4^{2-}, NO_3^-, K^+, NH_4^+, Ca^{2+} and Mg^{2+}) were also detected for both smoke extracts. Details can be found in Sect. S1 in the Supplement. These detection limits were determined based on three times the standard deviation of blank sample. The method detection limits ranged from 5–20 µg L^{-1} for anions and 0.5–2 µg L^{-1} for cations. The detection limits of Fe and Cu are 2.0 and 0.8 µg L^{-1}, respectively.

2.4 UV-vis and EEM analysis

The UV-vis absorption spectra were monitored using UV-vis spectrophotometer (Shimadzu, Japan) over wavelength range of 200–700 nm. The mass absorption coefficients (MACs, m^2 gC^{-1}), defined as absorbance normalized by WSOC concentration, were calculated as follows:

$$\mathrm{MAC}_\lambda = \frac{A_\lambda}{C \times L} \times \ln 10 \quad (1)$$

Where A_λ represent the absorbance at wavelength λ. C refers to the WSOC concentration of reaction solution. L is the optical path length (1 cm in this study).

The EEM spectra were recorded using a three-dimensional fluorescence spectrophotometer (FluoroMax Plus, HORIBA Scientific). Parallel factor analysis (PARAFAC) model was applied to EEM spectra to resolve the fluorescent compounds using the DOMFluor toolbox in MATLAB 2021b. Details of the determination and modeling procedures are provided in our previous study (Ye et al., 2025). Three fluorescence components (C1, C2 and C3) were identified from PARAFAC model. The fluorescence index (FI), humification index (HIX), and biological index (BIX) were further calculated to characterize the fluorescent properties of the samples. The calculation methods for these indicators were shown in the supplement and in our previous study (Ye et al., 2025).

2.5 FT-ICR MS measurement

The molecular compositions, degree of unsaturation, and aromaticity of WSOM were characterized using FT-ICR MS coupled with negative electrospray ionization (ESI-). Solid-phase extraction (SPE) was employed for sample pretreatment prior to FT-ICR MS determination, following procedures similar to those described in previous studies (Yang et al., 2025). Briefly, the reaction solution was adjusted to pH 2 and pass through SPE cartridges (Oasis HLB, Waters, USA) preconditioned with 15 mL methanol and 10 mL Milli-Q water. The retained organic matter was subsequently eluted with 10 mL methanol. The eluate was then concentrated to approximately 0.5 mL using a rotary evaporator and stored at −20 °C until analysis. Prior to analysis, the sample was re-dissolved in 4 mL of methanol and filtered through a 0.22 µm PTFE membrane. FR-ICR MS analysis was performed with a capillary voltage of 4.0 kV, and samples were introduced into the ESI source at a flow rate of 120 µL h^{-1}. Mass spectra were acquired over the m/z range of 150–800 Da. To improve the signal-to-noise ratio and dynamic range, each spectrum was averaged from 200 scans. Blank samples were analyzed under the same procedure. Notably, no water-insoluble precipitates larger than 0.22 µm were observed during photooxidation. However, filtration of the reaction solution through a 0.22 µm membrane prior to analysis may resulted in the loss of some newly formed oligomers.

The Composer software (Sierra Analytics, USA) was utilized to process the FT-ICR MS spectra and assign elemental compositions to recalibrated peaks, with a mass tolerance of ± 1.0 ppm and a signal-to-noise ratio (S/N) threshold of ≥ 4. Based on the assigned molecular formulas, WSOM compounds were categorized into four groups: CHO, CHON, CHOS, and CHONS. To evaluate the degree of unsaturation and aromaticity, double bond equivalent (DBE) and aromaticity index (AI) were calculated as follows:

$$\mathrm{DBE} = \frac{1}{2} \times (2c + 2 - h + n) \quad (2)$$

$$\mathrm{AI} = \frac{1 + c - 0.5o - s - 0.5h}{c - 0.5o - s - n} \quad (3)$$

The intensity-weighted averaged characteristic parameters can be expressed as:

$$P_{\mathrm{w}} = \left(\sum P_i \times I_i\right) / \sum I_i \quad (4)$$

where P represents DBE, AI, molecular weight (MW), oxygen-to-carbon (O / C) or hydrogen-to-carbon (H / C) ratio. P_i represents the corresponding parameter value for each individual compound I, and I_i represents the relative abundance of its molecular formula.

Molecular formulas were further classified into seven compound classes based on their H / C and O / C ratios (Ning et al., 2025): lipid-like ($1.5 < \mathrm{H/C} \leq 2.0$, $0 \leq \mathrm{O/C} \leq 0.3$); aliphatic -like ($1.5 < \mathrm{H/C} \leq 2.2$, $0.3 < \mathrm{O/C} \leq 0.67$); lignin-like ($0.67 < \mathrm{H/C} \leq 1.5$, $0.1 \leq \mathrm{O/C} < 0.67$); carbohydrate-like ($1.5 < \mathrm{H/C} \leq 2.5$, $0.67 < \mathrm{O/C} < 1.2$); unsaturated hydrocarbon-like ($0.67 < \mathrm{H/C} \leq 1.5$, $\mathrm{O/C} < 0.1$); unsaturated aromatic-like ($0.2 \leq \mathrm{H/C} \leq 0.67$, $\mathrm{O/C} < 0.67$), and tannin- ($0.6 < \mathrm{H/C} \leq 1.5$, $0.67 \leq \mathrm{O/C} \leq 1.2$). The saturated compounds were defined as the sum of lipid-like and aliphatic components.

2.6 High-resolution mass spectrometry analysis

High-resolution aerosol mass spectrometer (HR-AMS, Aerodyne Res. Inc.) was used to characterize the bulk chemical composition of aqSOA, including average elemental ratios (i.e., O / C and H / C) and some specific fragment ions. The average oxidation state of carbon ($\mathrm{OSc} = 2 \times \mathrm{O/C} - \mathrm{H/C}$) was used to index the oxidation degree of aqSOA. 10 mg L^{-1} ammonium sulfate was added into the solution as an internal standard for quantifying SOA mass concentration. The aqSOA mass yield was calculated as follows:

$$\begin{aligned}\text{aqSOA yield} &= \frac{[\mathrm{Org}]_t - [\mathrm{Org}]_0}{[\mathrm{WSOC}]_0 - [\mathrm{WSOC}]_t} \\ &= \frac{[\mathrm{Org}]_t \times \frac{[\mathrm{SO_4^{2-}}]_t}{[\mathrm{SO_4^{2-}AMS}]_t} - [\mathrm{Org}]_0 \times \frac{[\mathrm{SO_4^{2-}}]_0}{[\mathrm{SO_4^{2-}AMS}]_0}}{([\mathrm{WSOC}]_0 - [\mathrm{WSOC}]_t) \times M/12}\end{aligned} \quad (5)$$

Where $[\mathrm{SO_4^{2-}}]_t$ and $[\mathrm{SO_4^{2-}}]_0$ denote sulfate concentrations (mg L^{-1}) in the solution at irradiation time t and zero, respectively. Here, $[\mathrm{SO_4^{2-}}]_t$ was equal to $[\mathrm{SO_4^{2-}}]_0$ assuming sulfate was not loss during irradiation. The [Org] and $[\mathrm{SO_4^{2-}AMS}]$ denote the apparent concentrations of aqSOA and sulfate measured by HR-AMS. $[\mathrm{WSOC}]_t$ and $[\mathrm{WSOC}]_0$ were WSOC concentrations in the solution measured by TOC at irradiation time t and zero, respectively. M represents the averaged molecular weight of mixed solution which can be estimated by FT-ICR MS.

2.7 ROS determination based on electron paramagnetic resonance

Electron paramagnetic resonance (EPR) spectroscopy (Bruker EMXnano, Germany) was used to detect ROS. 5,5-Dimethyl-1-pyrroline N-oxide (DMPO) and 2,2,6,6-tetramethylpiperidine (TEMP) were used as spin-trapping agents for •OH and $^1O_2$ to identify the DMPO-OH adducts (1 : 2 : 2 : 1) and the TEMPO adducts (1 : 1 : 1), respectively (Hu et al., 2025b; Wang and Wang, 2020). The 10 mL of aqueous extracts were diluted into 100 mL using deionized water and pH was adjusted at 5.0 ± 0.1 with 0.1 M $\mathrm{H_2SO_4}$ solutions. Then 100 mM of two spin-trapping agents were added into the 50 mL of acidified aerosol extract solutions. After photodegradation of smoke extracts, 200 µL of solutions were transferred from the reaction solutions and immediately analyzed by EPR. The EPR parameters were set as following: modulation frequency of 100 kHz; center field of 3460 G, modulation amplitude of 1 G, microwave power of 25 mW, sweep width of 200 G, sweep time of 150 s, number of scans of 20.

3 Results and discussion

3.1 Comparison of fresh coal and maize smoke WSOM

Figure 1 showed the reconstructed FT-ICR mass spectra of WSOM for two fresh extracts samples. Based on the intensity of each negative ion, the average molecular formulas for coal and maize smoke extracts calculated as $\mathrm{C_{18.0}H_{24.0}O_{6.9}N_{0.90}S_{0.41}}$ and $\mathrm{C_{21.0}H_{21.7}O_{7.4}N_{0.86}S_{0.04}}$, respectively, showing higher C in maize smoke extracts, consistent with previous finding (Fan et al., 2016). In this study, these identified molecular formulas were classified into four main compound groups based on their compositions: CHO, CHON, CHOS, and CHONS. The relative abundances of the four groups were determined by normalizing the magnitude of each peak to the total magnitude of all identified peaks. Most peaks were located within the m/z range of 200–400. The greatest peak magnitudes were mainly distributed within the m/z range of 250–350. Distinct peak distribution patterns were observed for both smoke extracts. For example, several CHOS compounds with high relative abundance, such as $\mathrm{C_{12}H_{26}O_4S}$, $\mathrm{C_{17}H_{28}O_3S}$, $\mathrm{C_{18}H_{30}O_3S}$, were identified in the coal smoke extract, whereas the high-abundance CHO and CHON compounds, including $\mathrm{C_8H_{10}O_4}$, $\mathrm{C_7H_7NO_4}$, and $\mathrm{C_{18}H_{18}O_7}$ were predominant in the maize smoke extract. It should be noted that peak magnitude is not indicative of a compound's concentration in a sample due to inherent biases of C18 extractions and electrospray ionization efficiencies.

To better illustrate the differences in the •OH oxidation behavior between the two extracts, the concentrations of inorganic ions and transition metals (Fe and Cu) in the fresh WSOM were also measured, as shown in Table S1. It can be seen that the concentrations of $\mathrm{Cl^-}$ and $\mathrm{NH_4^+}$ ions in maize

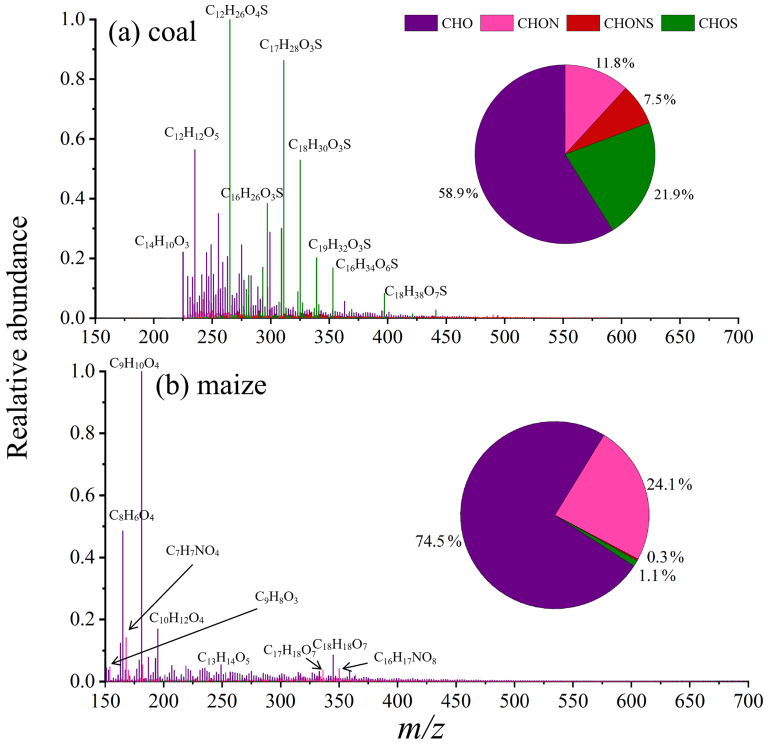

Figure 1. Reconstructed ESI(−) FT-ICR mass spectra of **(a)** coal and **(b)** maize smoke extracts colored by formula groups. The inserted pie charts show the percentage of four formula groups by intensity.

were much higher than those in coal, whereas the concentration of SO_4^{2-} ions in coal was higher than that in maize. During the photochemical reaction, the concentrations of these ions showed little change. In addition, the concentrations of Fe and Cu ions were very low, almost below the detection limits of the instrument. These results indicate that the influence of ions on the photochemical reaction can be neglected, especially that of Fe and Cu.

3.2 Optical properties during photooxidation of smoke extracts

3.2.1 Absorbance characteristics

Aqueous •OH oxidation of two smoke extracts – involving both photolysis and ROS oxidation reactions – can markedly alter their optical properties by degrading existing chromophores or generating new light-absorbing compounds. Figure 2a and b shows the UV-vis absorbance spectra in the range of 200–500 nm of the reaction solutions at varying irradiation time. Although the spectra were generally broad and featureless, noticeable differences in the absorption intensity were observed between coal and maize smoke. A distinct shoulder at 260 nm was observed in the spectra of maize smoke WSOM, attributed to π–π^* transitions of unsaturated double bonds (e.g., C = C and C = O) (Li et al., 2021), indicating the presence of fulvic acid-like chromophores. As the reaction progressed, overall decreases in absorbance (Fig. 2) were observed for both smoke extracts, which can be ascribed to the degradation of compounds containing carbonyl- and double bond groups. Tomaz et al. (2018) similarly reported that aqueous •OH oxidation of complex BB mixtures led to rapid depletion of phenolic compounds and formation of small organic acids. Consistent with these findings, photobleaching (i.e. decrease in light absorbance) is the most common effect observed upon irradiation of SOA or BrC in the aqueous phase (Jiang et al., 2023). The decreased light absorption was likely due to competing processes, including the formation of light-absorbing products and fragmentation yielding less absorptive compounds. Study by Chen et al. (2025) on molecular structure-dependent light absorption demonstrated that CHO compounds with low molecular weight and high aromaticity are primarily responsible for absorption in the 200–300 nm range, whereas CHON compounds (mainly nitroaromatics) and highly aliphatic structures play a dominant role in absorption above 365 nm. However, the present results differ from recent studies on aqueous SOA formation from the photooxidation of coal and rice straw smoke WSOM, which reported photoenhancement at wavelength above 360 nm (Cao et al., 2025). Such discrepancies may be attributed to differences in light sources, •OH concentrations, and the molecular composition of the smoke extracts. Clearly, different classes of compounds in smoke extracts exhibit distinct photochemical aging behavior, in-

cluding photoenhancement, photobleaching or a combination of both.

Changes in MAC_{365} are commonly used to track chromophore evolution since different chromophores exhibit varying light-absorbing ability. Figure 2c and d shows the variation of the MAC_{365} over reaction time for both smoke extracts. For both smoke extracts, MAE_{365} initially increased and then declined. The enhancement in light-absorbing can be mainly ascribed to two factors (Jiang et al., 2021). First, OH-addition to aromatic rings produces OH-rich compounds that act as chromophores (Lei et al., 2024). Second, the formation of dimers and larger oligomers extends π-conjugation, shifting absorption to longer wavelengths and enhancing light absorption. Generally, increased functionalization and oligomerization increased light absorption (Go et al., 2024; Vione et al., 2019). As the reaction proceeds, these intermediate chromophores transform into smaller, ring-opened molecules with weaker or negligible light absorption. The aqueous-phase photoaging of phenolic SOA also showed that light-absorbing properties of oxidation products were strongly time-dependent (Jiang et al., 2023). Additionally, photodegradation of WSOM can generate more volatile products, and their evaporation may reduce WSOC (Fig. S1), thereby influencing the light absorption per unit C mass. The final decrease in MAE_{365} can also be supported by the FT-ICR MS results (see Sect. 3.3). The observed decrease in lignin-like fractions, together with reductions in DBE and AI values, suggests the breakdown of these conjugated systems during aqueous photooxidation, leading to a decline in MAE_{365}. Meanwhile, the formation of more saturated compounds (e.g., lipid- and aliphatic-like species) further contributes to the decrease in MAE_{365}. In addition, the formation of small oxygenated CHO species (e.g., carboxylic acids or CHO_2 fragments from HR-AMS) with negligible absorbance at 365 nm dilutes the overall light-absorbing capacity. Another spectral parameter, E_2 / E_3 (the ratio of absorbance at 250 nm to that at 365 nm), further characterizes these changes. During the first hour of •OH oxidation, E_2 / E_3 decreased from 16 to 8 for coal smoke, indicating enrichment in high-molecular-weight chromophores with stronger light-absorbing capability. However, it increased from 12 to 22 for maize smoke extracts (Fig. S2). These contrasting E_2 / E_3 trends highlight distinct molecular transformations in WSOM for coal and maize smoke under •OH photooxidation.

3.2.2 Fluorescence properties

Fluorescence spectra provide more detailed molecular information than UV-vis spectra. For example, a red shift in the excitation–emission maximum typically indicates increased aromaticity and higher molecular weight (Tang et al., 2020). Figure 3a presents the EEM spectra of both smoke samples upon irradiation. We observed a rapid decrease in the characteristic fluorescence peak (EX / EM = 275 / 350 nm) within the first hour of the reaction. Concurrently, two new fluorescence peaks emerged at EX / EM = 325 / 400–500 and 225 / 400–500 nm, indicating the formation of humic-like chromophores. As the reaction progressed, the intensities of these newly formed peaks gradually declined. Consistently, HULIS-C concentrations increased during the initial 1–3 h for both smoke extracts, followed by a gradual decrease over time (Fig. S3). As shown in Fig. 3b, the total fluorescence intensity (EX = 250–450 nm, EM = 300–650 nm) decreased sharply within the first hour and then declined at a slower rate thereafter.

The HIX, BIX and FI were further employed to evaluate the degree of humification and freshness of organic matters. As suggested by Wu et al. (2021), an increased in HIX accompanied by decrease in BIX and FI can serve as indicators of enhanced oxidation of atmospheric WSOC. As shown in Fig. S4, the HIX value increased during the first hour and then decreased, suggesting that the formation of humic-like substances initially exceeded their subsequent degradation. Conversely, FI and BIX values decreased at the early stage of oxidation for both smoke samples (Fig. S4). In general, greater humification is associated with lower protein content, primarily due to a reduction in carbon-hydrogen compounds and a red shift in the fluorescence emission wavelength of more humified molecules. Conversely, a higher BIX indicates a higher contribution from protein-like and amino acid components.

The PARAFAC model identified three underlying fluorescent components, including one humic-like components (C1) and two protein-like component (C2 and C3) (Fig. 3). Component C1 is considered to be a humic-related substance, characterized by two peaks at EX / EM = 230 / 400–500 and 300 / 400–500 nm (Huang et al., 2025). C2 displays peaks at EX / EM = 250–300 / 300-350 nm, which can be attributed to tyrosine-like components. C3 (EX / EM =3 25 / 300 nm) is likely link to tryptophan-like components. As shown in Fig. 4, the proportion of C1–C3 in both maize and coal WSOM varied dynamically throughout photochemical processes. For coal WSOM, C1 fraction decreased, whereas C2 and C3 increased. In contrast, for maize WSOM, C2 gradually transformed into C1 at the first hour, resulting in opposite trends between the two components. This transformation likely reflects the formation of more oxygenated humic-like substances via OH-functionalization at the early stage, consistent with change trends of Hulis-C for maize smoke extracts (Fig. S3). This interpretation can be further confirmed by the increase in HIX values for maize smoke during the first hour of photooxidation (Fig. S4c).

For both smoke WSOM samples, the C3 component exhibited a gradual increase over time. The findings are in accordance with other's study on the photooxidation of WSOC emitted from rice straw combustion (Zhang et al., 2021). The stronger fluorescence intensity observed at EX / EM = 325 / 300 nm may correspond to low-ring PAHs and their derivatives, which are known to be produced in

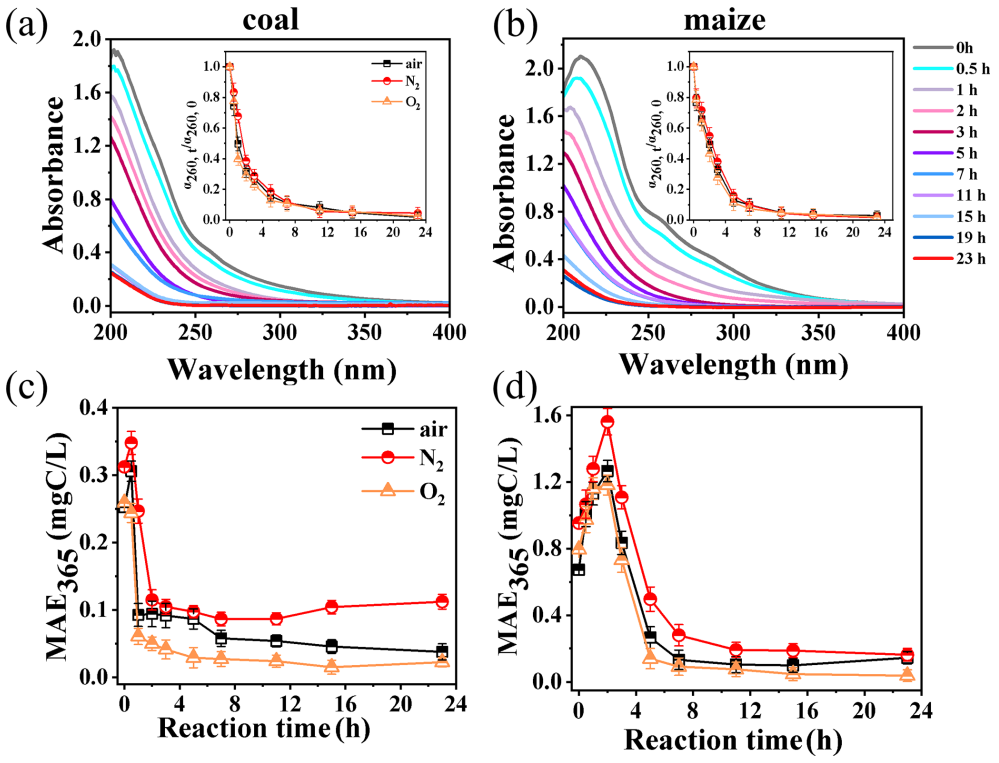

Figure 2. **(a, b)** The UV-vis absorption spectra under different irradiation time for coal and maize smoke extracts, and **(c, d)** MAE at 365 nm over photoaging time. The inset shows the change in absorbance at the wavelength of 260 nm compared to the spectra at time zero.

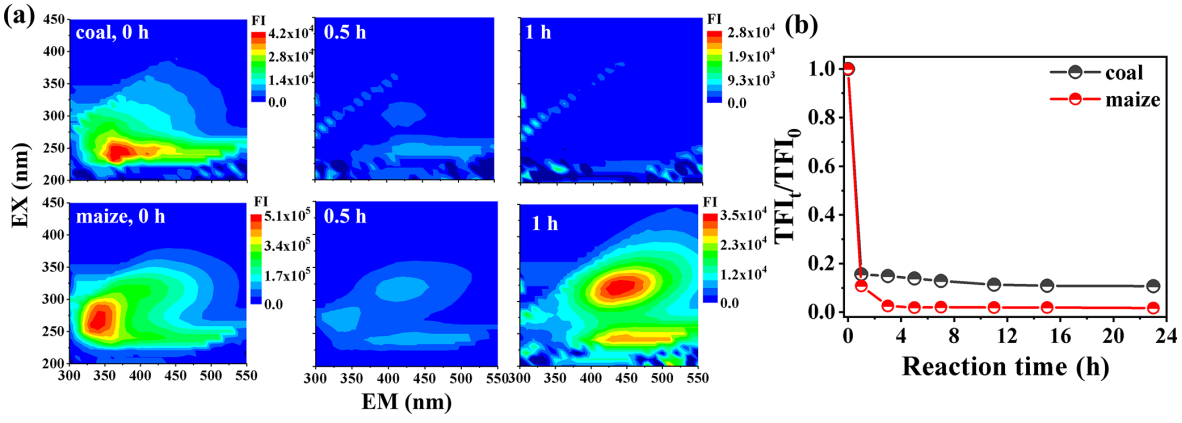

Figure 3. **(a)** Variation trend of EEM fluorescence spectra and **(b)** temporal profiles of total fluorescence intensity for two smoke extracts.

abundance during biomass pyrolysis or burning (Mahamuni et al., 2020). Overall, the EEM components varied depending on the types of smoke-derived WSOM.

3.3 Molecular composition of WSOM via FT-ICR MS

The intensity weighted average values of various molecular parameters – including molecular weight (MW), elemental ratios (H / C and O / C), DBE, AI – for maize and coal smoke extracts before and after photoaging were summarized in Table 1. As listed in Table 1, a total number of 5596 and 5107 molecular formulas were identified for fresh coal and maize extracts, respectively, within the m/z range of 100–600, indicating the complicated molecular compositions of WSOM. For coal WSOM, the MW decreased slightly 313 g mol^{-1} in the fresh sample to 296 and 288 after 11 and 23 h photooxidation, respectively. The MW for maize remained nearly unchanged during OH-photooxidation. The dominant species in both smoke extracts were CHO and CHON compounds, with higher abundance observed in maize than in coal smoke extract (Fig. 5). Molecular composition analysis further re-

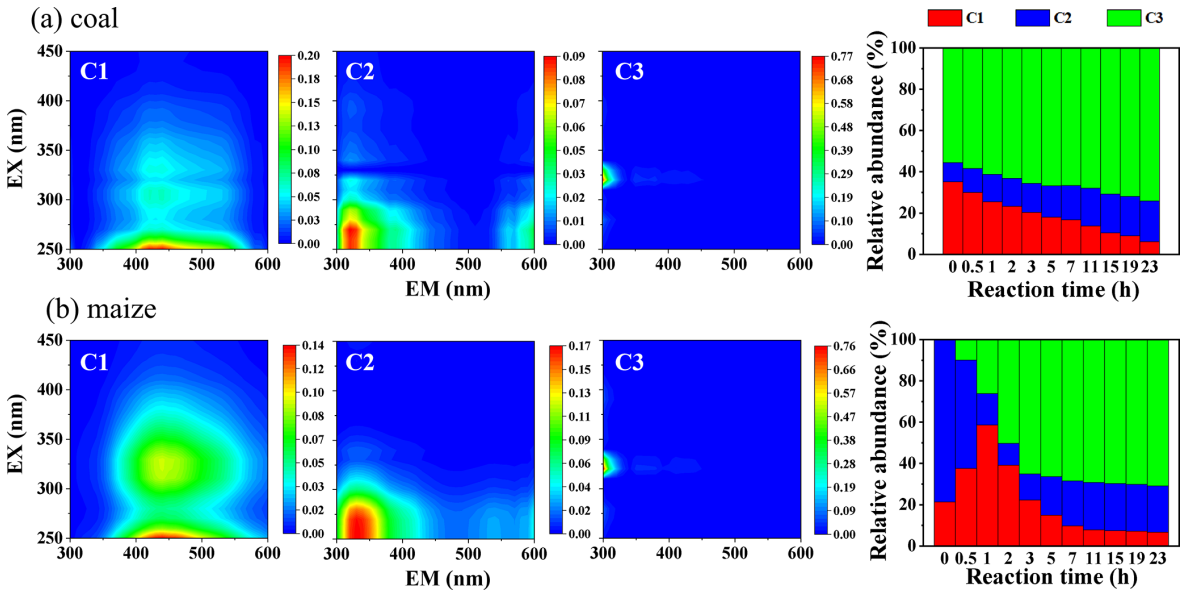

Figure 4. Three fluorescent components (C1–C3) of the smoke extracts identified by the EEM–PARAFAC model and variations in the relative contributions of each PARAFAC component of **(a)** coal and **(b)** maize smoke extracts with photoaging time.

vealed that maize smoke WSOM was largely composed of CHO and CHON, together accounting for 98.6 % of the total peak area. CHO compounds constituted more than half of all identified molecular formulas in both WSOM samples (74.5 % for maize and 58.9 % for coal). In contrast, S-containing compounds (CHOS and CHONS) were much more abundant in coal smoke extracts (29.4 % in total) than in maize (1.4 % in total). Similarly, previous studies reported that the fractions of S-containing CHOS and CHONS species in crop-derived WSOM were relatively low (3 %–9 % in peak area) (Li et al., 2024b). Interestingly, S-containing compounds in coal smoke decreased by nearly 50 % after photodegradation, whereas their abundance increased markedly in maize smoke extracts. Meanwhile, the proportion of CHON compounds in coal smoke increased under photoaging, which may be attributed to the photochemical transformation of CHONS species and/or the oxidation of reduced CHN compounds. Conversely, the CHON proportion in maize smoke decreases with reaction time, likely due to the progressive degradation of nitroaromatic compounds commonly present in biomass burning emissions (Lin et al., 2016).

The molecular-level parameters are summarized in Table 1. DBE values ranged from 2 to 9 for coal-smoke WSOM and from 2 to 11 for maize-smoke WSOM. The degree of unsaturation and aromaticity of molecular formulas can be valuated using the H / C ratio and DBE values, with lower H / C ratios and higher DBE indicating greater unsaturation and, to some extent, stronger aromatic character. As shown in Table 1, after 23 h of photooxidation, aged WSOM exhibited higher H / C ratios (1.75 vs. 1.32 for coal; 1.68 vs. 1.02 for maize), lower DBE values (3.85 vs. 7.12 for coal; 4.08

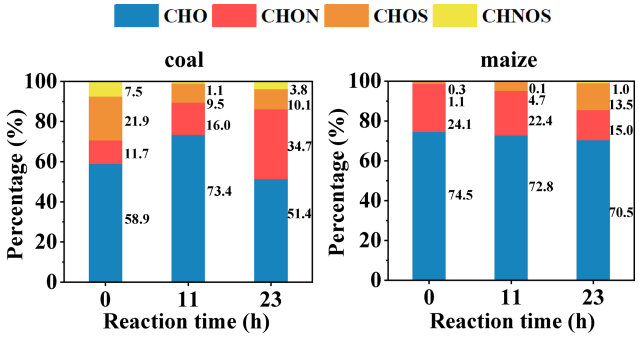

Figure 5. Change of relative abundance fraction of four groups (CHO, CHON, CHOS, and CHONS) with reaction time in both smoke extracts.

vs. 8.99 for maize), and reduced AI values (0.16 vs. 0.31 for coal; 0.16 vs. 0.48 for maize) compared to the fresh samples. These concurrent changes consistently indicate the breakdown of aromatic structures and an overall shift toward more saturated compounds. This trend agrees with previous findings from dark aqueous •OH oxidation of BB smoke WSOC reported by Fan et al. (2024).

At the molecular-class level, CHON compounds in maize smoke initially exhibit a relatively high average molecular weight (MW, 329.45 g mol^{-1}) and DBE (10.52). Upon photolysis, the average MW decreases to 301.07 (11 h) and 296.44 g mol^{-1} (23 h), while the DBE declines to 6.59 and 4.14, respectively. These changes reflect the progressive breakdown of conjugated structures and a corresponding reduction in aromaticity, consistent with the observed decrease in light absorbance (Fig. 2b). For coal smoke, a considerable

Table 1. Intensity-weighted average molecular parameters (MW, elemental ratios, DBE, DBE / C, AI) of coal and maize smoke WSOM before and after •OH photooxidation.

Sample	Time	Elemental composition	Formulas number	MW ($g\,mol^{-1}$)	DBE	AI	O / C	H / C	DBE / C
coal	0 h	Total	5596	312.98	7.12	0.31	0.38	1.32	0.45
		CHO	1728	300.23	8.16	0.38	0.36	1.16	0.52
		CHON	1695	323.12	8.77	0.43	0.49	1.25	0.54
		CHOS	702	310.03	3.60	0.10	0.31	1.74	0.23
		CHONS	1471	406.27	6.61	0.19	0.55	1.48	0.41
	11 h	Total	5157	296.35	4.58	0.17	0.45	1.57	0.34
		CHO	2066	286.35	4.61	0.16	0.47	1.54	0.35
		CHON	2029	312.31	4.10	0.16	0.40	1.68	0.31
		CHOS	816	343.04	4.93	0.16	0.29	1.62	0.29
		CHONS	246	329.73	6.45	1.01	0.86	1.63	0.54
	23 h	Total	5072	288.32	3.85	0.16	0.27	1.75	0.25
		CHO	1348	262.69	4.04	0.15	0.26	1.66	0.28
		CHON	1970	304.36	2.03	0.07	0.25	1.99	0.14
		CHOS	723	313.19	4.80	0.17	0.31	1.67	0.27
		CHONS	1031	398.63	7.04	0.33	0.52	1.63	0.39
maize	0 h	Total	5107	286.90	8.99	0.48	0.40	1.02	0.62
		CHO	2143	273.62	8.56	0.46	0.40	1.02	0.61
		CHON	2772	329.45	10.52	0.54	0.40	0.98	0.66
		CHOS	107	248.21	4.61	0.22	0.46	1.37	0.47
		CHONS	85	317.32	7.31	0.28	0.56	1.13	0.61
	11 h	Total	6027	288.84	5.44	0.21	0.55	1.40	0.44
		CHO	2643	283.95	5.19	0.19	0.56	1.41	0.42
		CHON	2954	301.07	6.59	0.30	0.57	1.29	0.54
		CHOS	395	305.41	3.69	0.12	0.35	1.83	0.20
		CHONS	35	317.42	10.37	0.45	0.23	1.19	0.54
	23 h	Total	5147	285.81	4.08	0.16	0.25	1.68	0.27
		CHO	2647	277.01	4.20	0.16	0.23	1.65	0.27
		CHON	1995	296.44	4.14	0.19	0.28	1.69	0.30
		CHOS	400	312.24	2.94	0.09	0.34	1.86	0.18
		CHONS	105	393.70	10.63	1.03	0.49	1.11	0.67

fraction of CHONS species undergoes transformation into CHON compounds with lower aromaticity and DBE during photolysis. This conversion increases the relative abundance of CHON species while contributing to a decrease in overall molecular weight. In addition, the MW of CHO compounds in coal smoke decreases progressively with photolysis. In contrast, maize-smoke WSOM is dominated by CHO compounds, whose MW remains relatively unchanged during photolysis, resulting in only minor variation in the bulk molecular weight. This contrast primarily reflects differences in the initial WSOC compositions between coal and maize smoke. Overall, the marked decreases in AI and DBE for CHON compounds in both smokes indicate substantial loss of aromaticity, which in turn contributes to the reduction in light absorption.

Additionally, the O / C increased from 0.38 to 0.45 for coal and from 0.40 to 0.55 after 11 h of oxidation, followed by a decrease to 0.27 and 0.25 at 23 h, respectively. This tread indicates a transformation from OH-functionalization to fragmentation as photooxidation progressed. A decrease in DBE per carbon (DBE per C) was observed after 23 h of photodegradation – from 0.45 to 0.25 for coal and 0.62 to 0.27 for maize – further confirming the transformation of refractory aromatic-condensed structures into more polar and readily degradable small molecules. Figure S5 shows the relationship between DBE values and C atom numbers for four compound groups identified by FT-ICR MS.

The van Krevelen diagram (Fig. 6), which plots the O / C ratio as the x-axis and the H / C ratio on the y-axis, was used to elucidate the molecular distribution. For clarity, the corresponding detailed values were listed in Table S2. Lignin-like compounds dominated both coal and maize smoke WSOM, accounting for 58.2 % and 93.1 % of total intensity, respectively, indicating a greater abundance of phenolic organic

species in maize smoke. Previous study also showed that CHO formulas were mainly lignin-pyrolysis products (Song et al., 2018). After photoaging, the lignin-like fraction decreased significantly, reflecting the degradation of aromatic phenolic species. Given that most lignin-like compounds possess strong light-absorbing properties, their decomposition directly contributed to the observed decrease in absorbance. In contrast, the intensity of saturated compounds (sum of lipids and aliphatic components) increased substantially after OH-induced photooxidation, from 33.8 % to 51.2 % at 23 h for coal and from 2.4 % to 69.8 % for maize. These observations suggest a significant increase in saturated aliphatic and O-enriched compounds after •OH photooxidation.

As listed in Table S2, the initial increase followed by a decrease (from 11.2 % to 1.1 % for coal and 31.8 % to 2.1 % for maize smoke) in tannin-like compounds suggests that radical coupling, condensation, or addition reactions likely occurred during the early stage of the reaction, leading to a higher O / C ratio at 11 h compared to the fresh sample.

Condensed aromatic molecules, characterized by low H / C and O / C ratios but high AI, showed a slight decrease with photoaging, indicating the partial degradation of highly aromatic structures. Overall, the reduction in aromatic and lignin-like compounds aligns with the observed decline in the light-absorbing properties (see Sect. 3.2.1). In all, aromatic and lignin-like compounds were continuously transformed into lipid- and aliphatic-like compounds. During the initial stage (first 5 h), carbohydrate-like substance such as oxalate were generated (Fig. S6), but their abundance subsequently decreased, consistent with the pH variation that first declined (initial 3 h) and then increased again (Fig. S7). The formation of carboxylic acids can be further confirmed later by identifying their characteristic fragment ions using HR-AMS.

To further elucidate the photooxidation behaviors of both smoke extracts, the number proportions of resistant, degraded and newly produced molecules were summarized in Table S3. After 11 h of irradiation, 55.1 % and 58.2 % of the total formulas in fresh coal and maize, were degraded, resulting in 51.3 % and 64.6 % newly formed formulas. From 11 to 23 h, the numbers of newly produced and degraded molecules increased slightly for coal but decreased for maize. Figure 7 illustrates the O / C vs. H / C distributions of degraded and newly formed compounds after 11 and 23 h of photodegradation. For coal, most degraded compounds were located in high O / C regions, whereas some newly formed species with much lower O / C and higher H / C were likely associated with unsaturated hydrocarbons and lipid-like species. In contrast, maize exhibited a marked shift from low to high O / C and H / C compounds at 11 h, resulting in an increase in average O / C ratio. This trend suggests that maize compounds mainly underwent functionalization during the first stage – introducing oxygen-containing groups without breaking the carbon skeleton, thereby increasing O / C and slightly lowering or maintaining H / C. The shift toward higher O / C ratios in the van Krevelen diagram further supports the progression from aromatic to more oxygenated and saturated compounds for maize smoke WSOM.

Overall, these results reveal distinct degradation pathways and product characteristics for coal and maize smoke extracts.

3.4 AqSOA composition and mass yield

The aqSOA spectra exhibited higher mass fractions of $CxHy^+$ and $CxHyO_1^+$ ions but lower fractions of $C_xH_yN_p^+$ and $C_xH_yO_xN_p^+$ ions (Fig. 8). For corn-derived aqSOA, the fractions of $C_xH_y^+$ and $CxHyO_1^+$ both decreased by approximately 10 % with increasing photolysis time, while $CxHyO_2^+$ increased substantially from 15.95 % to 29.96 % after 23 h of photoreaction. In contrast, for coal-derived aqSOA, the fraction of $CxHyO_1^+$ increased with irradiation time, while no corresponding increase in $CxHyO_2^+$ was observed. This suggests that the overall oxidation degree of coal-derived aqSOA did not increase significantly relative to that prior to irradiation.

Table S4 summarizes the chemical properties, mass concentration and yield of the formed aqSOA and their evolution during the photoreaction. During the first 5–7 h, both $f44$ and OSc values increased, indicating a progressive enhancement in the oxidation state of aqSOA for both samples. In contrast, the H / C ratio exhibited only minor changes throughout the reaction, suggesting relatively stable bulk hydrogen content despite ongoing oxidation. A comparison between the two systems further reveals that maize-derived aqSOA undergoes a more pronounced increase in oxidation at the early stage, likely driven by functionalization reactions. As photochemical processing continues, however, a slight decline in oxidation is observed, which can be attributed to fragmentation processes. This trend is less evident in coal-derived aqSOA, highlighting differences in their underlying transformation mechanisms. Notably, the significantly higher O / C ratios and OSc of maize-derived aqSOA compared to those of the precursors suggest that aqueous-phase processing can serve as an effective source of oxygenated SOA in regions influenced by biomass burning emissions. The value of $f43$ remained relatively low value (less than 0.1) and is therefore not discussed further.

For coal samples, the aqSOA mass concentration ranged from 50.77 to 126.95 mg L^{-1}. It reached a minimum at 11 h and subsequently increased to 126.95 mg L^{-1} at 23 h. Correspondingly, the aqSOA mass yield peaked at 148.44 % at 1 h, continuously decreased to 1.87 % within 9 h, and then increased again to 33.91 % at 23 h. The aqSOA mass yield of maize was significantly lower (less than 10 %) than that of coal samples, indicating that coal sample is more efficient at generating low-volatility species compared to maize.

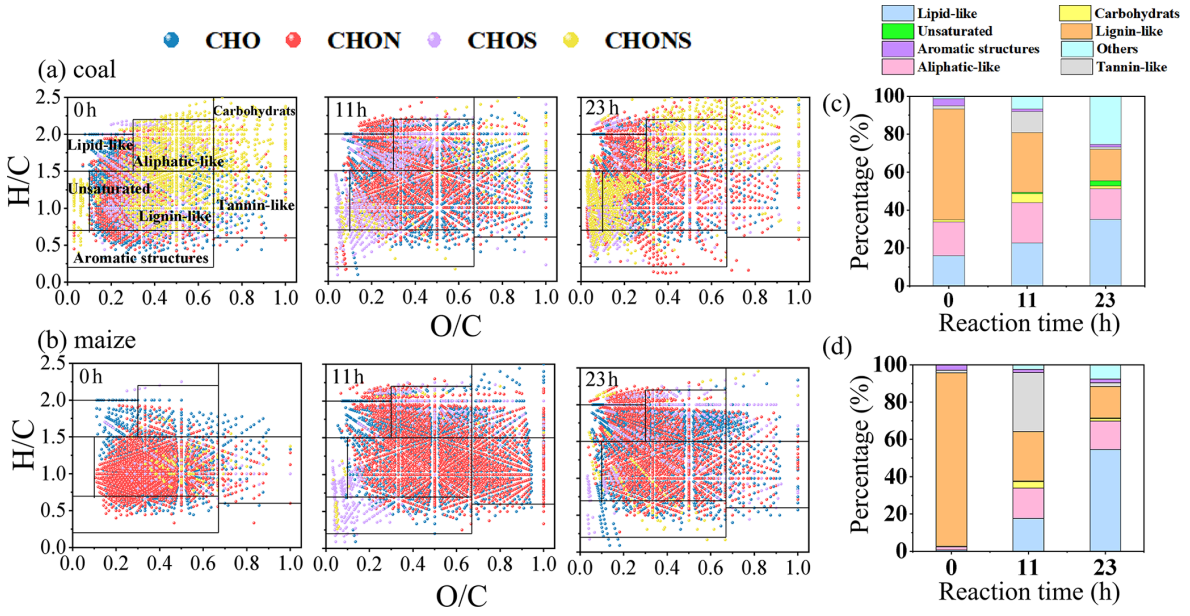

Figure 6. **(a, b)** Van Krevelen diagrams of four groups (CHO, CHNO, CHOS, and CHNOS) and **(c, d)** Intensity-weighted fractions of seven major molecular classes. Saturated compounds represent the sum of lipid-like and aliphatic components. Unsaturated represents unsaturated hydrocarbons.

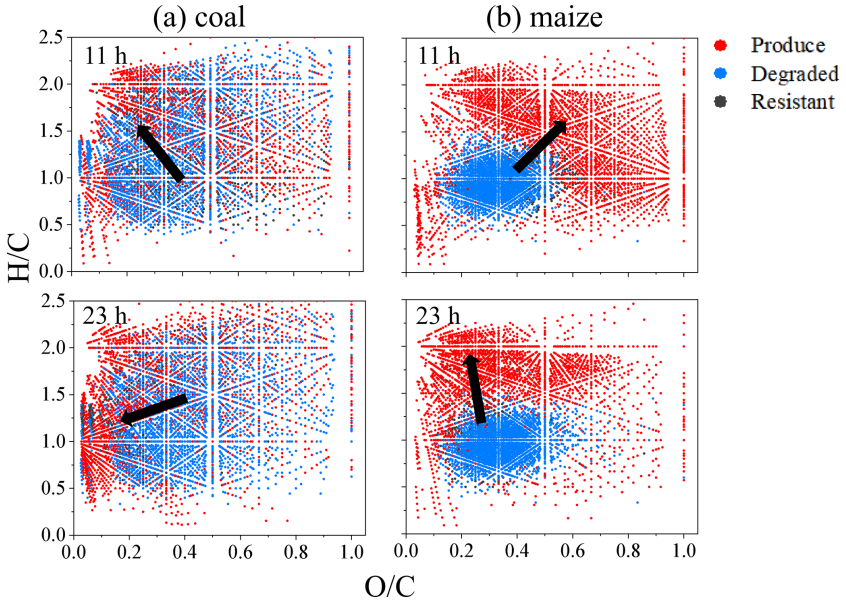

Figure 7. Van Krevelen diagrams of resistant, degraded and produced formulas in WSOM derived from **(a)** coal and **(b)** maize burning before and after OH photooxidation.

The possible reasons why coal-derived aqSOA is higher than that from maize are as follows. First, the fresh coal-derived CHOS compounds are dominated by species such as $C_{17}H_{28}O_3S$ and $C_{18}H_{30}O_3S$, which are mainly organosulfates. These compounds have relatively high saturation and stability, and undergo little change upon photolysis, resulting in a high SOA mass yield measured by HR-AMS. In contrast, maize-derived WSOM is primarily composed of lignin-like substances with high DBE values, which are more susceptible to OH functionalization, forming saturated fatty acids or polyhydroxy acids (e.g., $C_9H_{18}O_6$ and $C_9H_{10}O_7$). These products can further undergo fragmentation into smaller, more volatile products (e.g., low-molecular-weight acids), leading to a lower aqSOA mass yield.

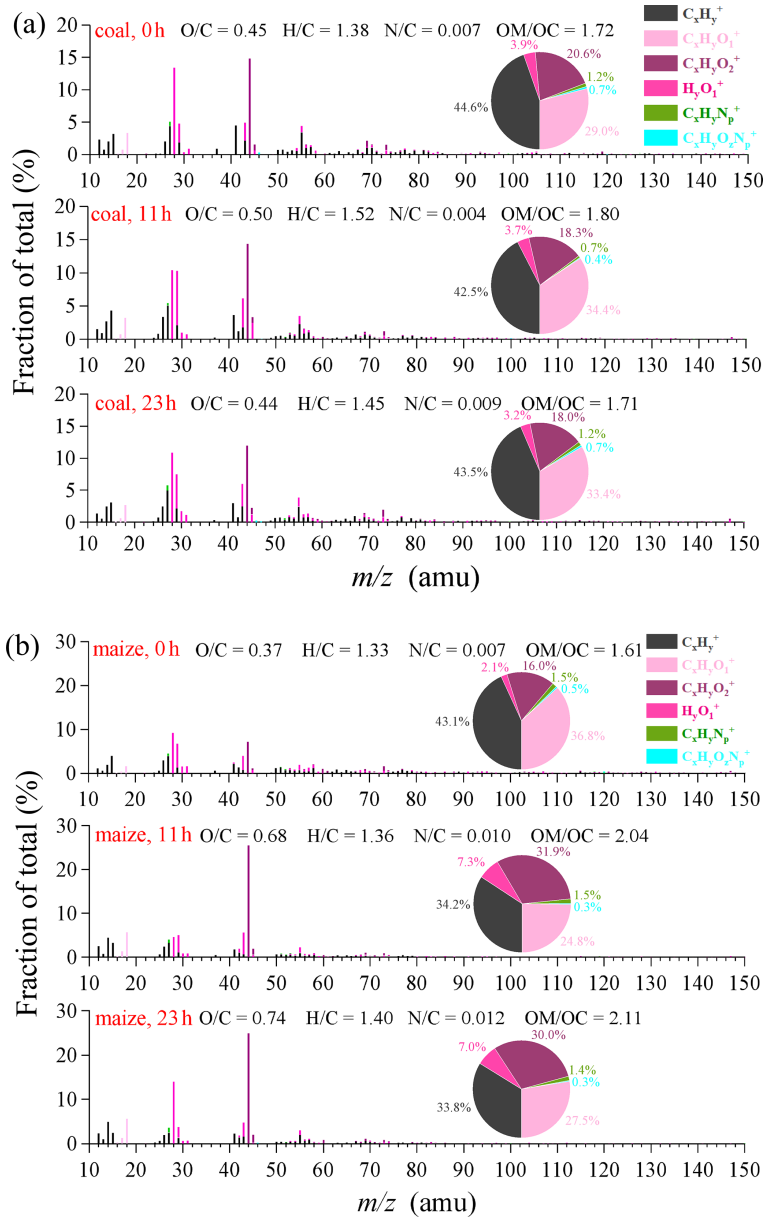

Figure 8. High-resolution MS profiles for aqSOA products at 0, 11 and 23 h for **(a)** coal and **(b)** maize. The peaks in the mass spectra are color-coded according to six ion categories: $C_xH_y^+$, $C_xH_yO_1^+$, $C_xH_yO_2^+$, $H_yO_1^+$, $C_xH_yN_p^+$ and $C_xH_yO_xN_p^+$ ions. The inserted pie charts denote the mass fraction of each ion family to the total MS.

The significant formation of carboxylic acids during the first 9 h of photoreaction is further evidenced by the Van Krevelen diagram (H / C versus O / C), in which aqSOA evolves along a slope of approximately −1 throughout the photooxidation process (Fig. S8). Consistently, the CHO_2^+ ion in the aqSOA AMS spectra – commonly used as a tracer for carboxylic functional groups – exhibits a continuous increase during the first 5 h of photoreaction (Fig. S9). After 3–9 h of reaction, the concentration of CHO_2^+ decreases, accompanied by a decline in $f44$. A plausible explanation is the occurrence of fragmentation reactions, during which the oxidation products initially formed through oligomerization or functionalization decompose into smaller, more oxidized species. This trend has also been reported in previous studies on the photooxidation of phenolic carbonyls (Jiang et al., 2021).

3.5 DTT analysis

Aqueous photochemical aging of BB smoke can also alter its toxicity. The oxidative potential of the reaction solutions was evaluated using the dithiothreitol (DTT) assay, as de-

scribed in our previous work (Ye et al., 2025). As shown in Fig. 9a, based on the DTT consumption rate (OP^{DTT}), OH-initiated photooxidation of smoke extracts led to an increase in OP^{DTT} during the first 1 h. Upon prolonged photoaging, the OP^{DTT} value decreased to 0.15 µM DTT min^{-1} after 23 h, slightly lower than the corresponding initial values. Previous research results also suggested that aqueous OH oxidation of WS-BBOA components generally leads to a final reduction in OP^{DTT} (Wong et al., 2019; Jiang and Jang, 2018) during prolong irradiation, consistent to our findings. The temporal variation pattern of OP^{DTT} is comparable to that observed for aqueous oxidation of soybean straw extracts (Ye et al., 2025), but opposite to that of 4NC photodegradation (Lei et al., 2025). The DTT activity is likely associated with light-absorbing and fluorescent substances containing large conjugated electron systems, which can transfer electrons to participate in catalytic reaction, thereby contributing to DTT activity (Chen et al., 2019). The reduction in DTT activity after 23 h agrees with the decrease of lignin-like and aromatic compounds revealed by FT-ICR MS analysis.

Given that aqueous •OH oxidation did not significantly reduce the total WSOC concentrations, the decrease in OP^{DTT} is likely attributed to the formation of non- or less DTT-active components. However, total WSOC decreased significantly upon aging; consequently, the OP^{DTT} normalized by WSOC increased over irradiation time, suggesting the possible formation of secondary toxic organic species during the aging processes. Previous published studies have also showed that photochemical aging of fresh particles can either enhance or diminish toxicity, depending on their sources and oxidation conditions (Fang et al., 2024). To further characterize the ROS-generation potential of WSOM from different combustion sources, we calculated the WSOC-normalized DTT consumption rate (OP^{DTT}_{WSOC}, OP^{DTT} divided by WSOC). The results showed that the mass-normalized DTT consumption rates gradually increased and reached a plateau at 132 and 82 pmol min^{-1} $µg^{-1}$ for maize and coal smoke extracts, respectively, similar to finding from Wong et al. (2019). These values are higher than those reported for water extracts from $PM_{2.5}$ aerosol (22–68 pmol min^{-1} $µg^{-1}$) (Verma et al., 2012). Based on the molecular-level differences after •OH photooxidation, the reasons for the OP^{DTT}_{WSOC} changes induced by OH-photolysis in coal and maize are likely different. For coal, the increase in OP^{DTT}_{WSOC} may primarily result from the formation of CHON compounds after photolysis, whereas for maize, the increase is probably due to the production of more quinone species or OH addition products during the reaction (Tang et al., 2025; Wong et al., 2019).

Unfortunately, due to the limitations of current analytical techniques, it remains challenging or even impossible to attribute the observed DTT variation trends to specific molecular species.

3.6 ROS contribution and reaction mechanism

3.6.1 ROS concentration and relative contribution

Hydrogen peroxide can undergo photolysis to generate •OH, which effectively break down chromophores, thereby decreasing light absorption. The OH radicals can oxidize most organic species, leading to a sharp decrease in both WSOC and absorbance during the initial reaction stage.

According to previous studies (Arciva et al., 2022), when the concentration of the BB mixture reaches 12 mg C L^{-1}, the concentration of photosensitizers in solution can exceed several millimoles. This suggests that the smoke samples in the present study likely contains substantial amounts of photosensitizing compounds. Upon exposure to sunlight, these photosensitizer (denoted as PS) absorb photons and transition to their triplet excited state ($^3PS^*$). The excited triplet states can subsequently react with O_2 to produce various ROS, including $^1O_2$, superoxide ($O_2^{\bullet-}$), hydroperoxyl radical ($•HO_2$), and •OH, through H-abstracting, electron transfer and energy transfer processes. These ROS species actively participate in subsequent photooxidation reactions.

$$H_2O_2 \rightarrow 2•OH \quad (6)$$

$$H_2O_2 + OH \rightarrow 2HO_2 + H_2O \quad (7)$$

$$HO_2 \rightarrow O_2^{\bullet-} + H^+ \quad (8)$$

$$PS + h\nu \rightarrow {}^1PS^* \rightarrow {}^3PS^* \quad (9)$$

$${}^3PS^* + {}^1PS^* \rightarrow PS^{\bullet+/\bullet-} \quad (10)$$

$${}^3PS^* + O_2 \rightarrow PS + {}^1O_2 \quad (11)$$

$$PS^{\bullet-} + O_2 \rightarrow PS^+ + O_2^{\bullet-} \quad (12)$$

$$O_2^{\bullet-} + 2H^+ \rightarrow H_2O_2 + O_2 \quad (13)$$

$${}^3PS^* + R-H \rightarrow PS-H• + R• \quad (14)$$

$$PS-H• + O_2 \rightarrow PS + •O_2 \quad (15)$$

$$2•O_2 \rightarrow H_2O_2 + O_2 \quad (16)$$

According to method described in Sect. 2.7, the steady-state concentrations of •OH (denoted as $[•OH]_{ss}$) and $[^1O_2]$ (denoted as $[^1O_2]_{ss}$) were determined using EPR. The distinct 1 : 1 : 1 triplet EPR signal characteristic of $^1O_2$ and 1 : 2 : 2 : 1 quartet signal of •OH confirmed the generation of $^1O_2$ and •OH, with signal intensities increasing as the reaction time progressed (Fig. S10). It should be noted that EPR-based spin-trapping methods have inherent limitations. For example, spectral overlap and background signals may affect the resolution and accuracy of peak assignment. Furthermore, certain short-lived or low-reactivity ROS may not be effectively captured by the selected spin traps. Therefore, the reported ROS contributions should be interpreted as semi-quantitative estimates rather than absolute concentrations

Then, a chemical probe method was employed to further quantify the concentrations of •OH and $^1O_2$. Benzoic acid (BA) was used as the •OH probe compound according to previously established protocol (Hu et al., 2025b). Briefly,

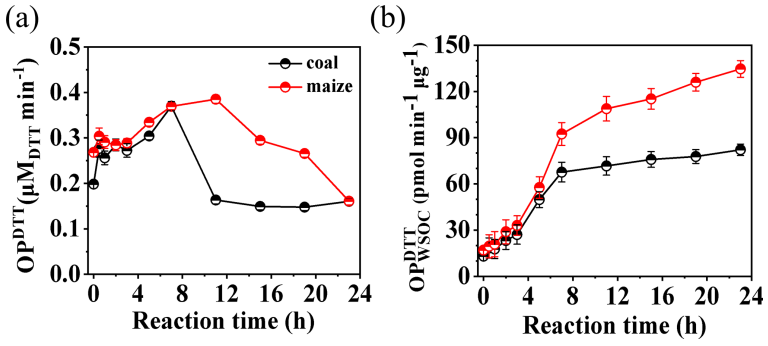

Figure 9. **(a)** Temporal evolution of DTT consumption rate and **(b)** WSOC-normalized DTT activity for both smoke extracts during aqueous OH photooxidation.

six different concentration of BA (5, 10, 15, 20, 30, 40 and 50 µM) were added to separate aliquots of the same extract. After illuminating for time t, the residual BA concentration was monitored by UPLC-PDA. A linear regression of $-\ln[BA] / \ln[BA]_0$ versus reaction time t yielded the pseudo-first-order rate constant (k_{BA}) (Fig. 10a, b). By plotting the reciprocal ($1 / k_{BA}$) against [BA], the intercept was obtained (Fig. 10c), from which $[OH]_{ss}$, was determined by dividing the intercept by the second-order rate constants $k_{BA,\,OH}$ (Lei et al., 2023). The $k_{BA,\,OH}$ is strongly dependent on pH value. Under low pH conditions, benzoic acid predominantly exists in its molecular form (BA), whereas at high pH it is mainly present as the deprotonated species (benzoate, BA^-). These different forms exhibit distinct reactivity toward •OH. According to the literature (Arakaki et al., 2013), when pH > 6, BA^- is the dominant species, with a rate constant $k^-_{BA,\,OH} = 6.0 \times 10^9\ M^{-1}\ s^{-1}$; when pH < 4, the molecular form dominates, with $k_{BAOH} = 1.8 \times 10^9\ M^{-1}\ s^{-1}$. In this study, the initial pH values of coal and maize samples were 6.79 and 5.83, therefore, $5.1 \times 10^9\ M^{-1}\ s^{-1}$ (Lei et al., 2023) was adopted to calculate the steady-state concentration of OH. The estimated $[OH]_{ss}$ were 9.11×10^{-14} and 8.58×10^{-14} M for coal and maize smoke extracts, respectively (Fig. 10) – values comparable to those typically observed in atmospheric cloud droplets (Arakaki et al., 2013; Li et al., 2023).

The steady-state concentrations of $^1O_2$ and $^3C^*$ were also quantified by monitoring the decay of furfuryl alcohol (FFA) and syringol (SYR) under pseudo-first-order kinetics (Fig. 10d–f), following previously established procedures (Li et al., 2024a). Considering the relatively high •OH concentration in the mixed system, potential interference may occur when using FFA as a probe, since it can react with both •OH ($k_{FFA,\,OH} = 1.5 \times 10^{10}\ M^{-1}\ s^{-1}$) and $^1O_2$ ($k_{FFA,\,^1O_2} = 1.2 \times 10^8\ M^{-1}\ s^{-1}$). To eliminate this interference, excess methanol was added to completely quench •OH ($k_{MeOH,\,OH} = 1.0 \times 10^9\ M^{-1}\ s^{-1}$) before employing FFA to determine the $^1O_2$ concentration. The results (Fig. 10) showed that the $[^1O_2]_{ss}$ values were 3.48×10^{-13} and 1.8×10^{-12} M for coal and maize smoke extracts, respectively, higher than that reported for 5 mg C L^{-1} of SOA extracts (3×10^{-14} M) (Manfrin et al., 2019). Generally, $^1O_2$ was born by triplets thus tightly linked to $^3C^*$. The significantly higher $^1O_2$ concentration observed in maize smoke extracts – approximately six times that of coal smoke extracts – indicates a greater abundance of triplet-state precursors in maize-derived WSOM. Similarly, SYR was employed as a chemical probe due to its high reactivity with triplets ($k_{SYR,\,^3C^*} = 3.9 \times 10^9\ M^{-1}\ s^{-1}$) (Ma et al., 2023). Based on its pseudo-first-order decay kinetics, the steady-state concentrations of $^3C^*$ in the maize and coal systems were determined to be 9.0×10^{-13} and 7.05×10^{-13} M, respectively (Fig. 11f).

The steady-state concentrations determined in our system are approximately one order of magnitude higher than those reported in aqueous PM extracts illuminated with 365 nm lamps (e.g., $\sim 10^{-13}$ M for triplets) (Bogler et al., 2022). Data from Ma et al. (2024) also showed the concentrations of •OH, $^1O_2$, and $^3C^*$ in $PM_{2.5}$ extracts range from $(0.2–4.7) \times 10^{-15}$ M, $(0.7–45) \times 10^{-13}$ M, and $(0.03–7.9) \times 10^{-13}$ M, respectively. This significant difference is mainly attributed to the addition of 10 mM H_2O_2 in our experiments. Given an estimated average molecular weight of 300 g mol^{-1} for WSOM, the resulting molar ratio of H_2O_2 to WSOM (15 mg C L^{-1}) is approximately 200 : 1. This substantial excess of H_2O_2 provides a high concentration of •OH, sufficient to extensively oxidize WSOM and explaining why our •OH levels are orders of magnitude greater than those in typical PM extracts (Ma et al., 2024).

Consequently, the degradation of WSOM in our system is predominantly driven by •OH oxidation, with minor contributions from other reactive species. Furthermore, the concentrations of $^1O_2$ and $^3C^*$ were also slightly higher than those in ambient PM extracts (Ma et al., 2024), likely because our simulated combustion samples contained higher levels of phenolic compounds and PAHs, which are known precursors for these species.

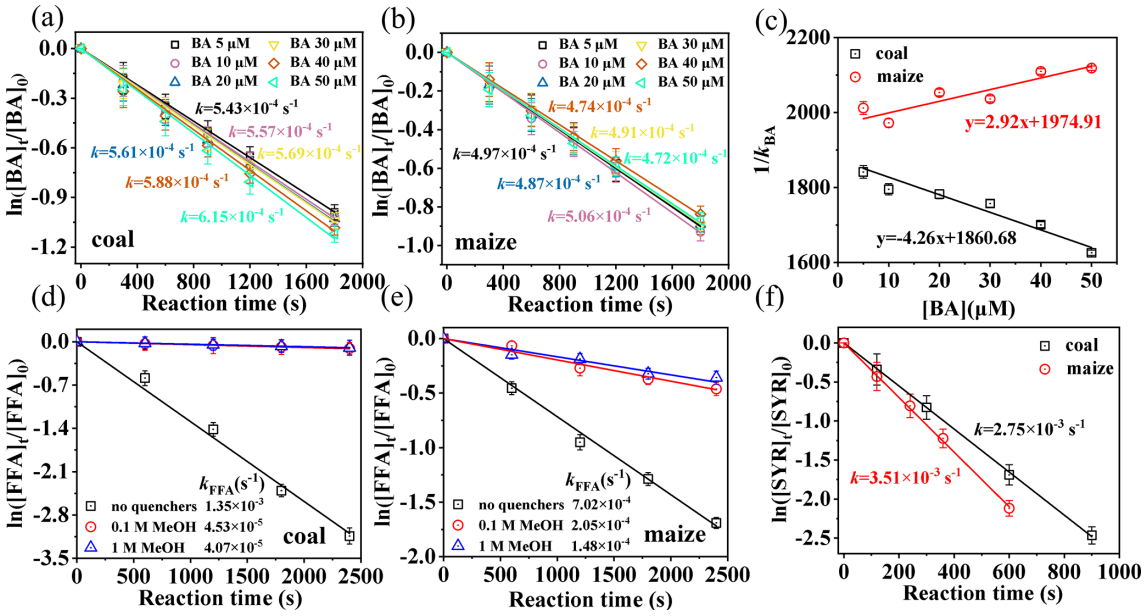

Figure 10. Loss of **(a, b)** BA, **(d, e)** FFA, **(f)** SYR and **(c)** plot of $1 / k_{BA}$ and BA concentration.

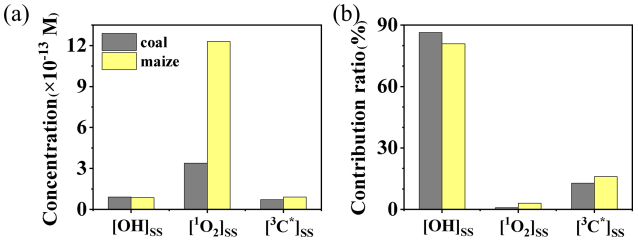

Figure 11. ROS steady-state contribution and their contribution to WSOM photodecay.

To elucidate the reaction mechanism, the role of different ROS in the photodecay and light absorbance of smoke extracts were examined. The absorption spectra of smoke extracts with and without 0.1 M methanol (•OH quencher) were compared (Fig. S11). A molar ratio of 2000 : 1 (MeOH : WSOM) was employed, assuming an average molecular weight of 300 g mol^{-1}, to ensure complete scavenging OH given the comparable second-order rate constants of MeOH and WSOM with •OH (Liu-Kang et al., 2024). As shown in Fig. S11, absorbance decay rate decreased markedly, especially within the first hour, indicating that •OH play a dominant role in the photodacay of the extracts.

To further assess the contributions of individual ROS, comparative experiments were conducted under N_2-, air-, and O_2-saturated conditions. Under N2 saturation, secondary oxidants such as HO_2•and •OH were largely excluded due to the absence of oxygen. The changes in WSOC indicate that direct photolysis in both smoke extracts was much weaker than •OH oxidation. Under •OH oxidation, the WSOC loss under N2-saturated conditions was much lower than that under O_2- and air-saturated conditions (Fig. S12), whereas in direct photolysis, the differences among the three gas conditions were negligible (Fig. S13). This suggests that O_2 plays a crucial role only for •OH oxidation.

Previous studies have reported that $^3C^*$-initiated photooxidation of phenolic compounds proceeds most rapidly under N_2-saturated conditions (Lei et al., 2023). In contrast, our results showed the fastest degradation under O_2-saturated and the slowest under N_2, implying that $^3C^*$ is not the dominant oxidant in our system. This conclusion is further supported by the comparable WSOC degradation observed for coal and maize smoke extracts. Theoretically, if $^3C^*$ were the primary oxidant, maize extracts would be expected to exhibit a much higher WSOC degradation owing to their greater content of photosensitizers, as indicated by the higher lignin-like compounds in maize (Sect. 3.3).

The relative importance of individual ROS in WSOM photodecay was evaluated by multiplying their corresponding second-order rate constants with their steady-state concentrations. Thus, we estimated the relative role in smoke WSOM photodecay. Given that reaction rates of WSOC with •OH and $^3C^*$ were 3.8×10^8 and 7.2×10^7 M^{-1} s^{-1}, whereas $^1O_2$ reacts much more slowly (10^5 M^{-1} s^{-1}) (Ma et al., 2024), the contributions were calculated (Fig. 10b). For coal smoke extract, •OH, $^3C^*$, $^1O_2$ accounted for approximate 86.4 %, 12.8 % and 0.8 % of the total oxidation, respectively. A similar pattern was observed for maize smoke extracts (80.9 %, 16.0 % and 3.1 %), with the overall contribution order of •OH > $^3C^*$ > $^1O_2$. Although $^1O_2$ exhibited the highest steady-state concentration, its low reactivity limited its overall contribution, consistent with previous findings (Zhang et al., 2024). According to earlier reports (Tang et

al., 2025), when the concentration of the BB-derived mixture reaches 12 mg C L^{-1}, the concentration of photosensitizers in solution can exceed several millimoles. Therefore, $^3C^*$ also plays an important and non-negligbile role in the photodegradation of both smoke WSOM.

Surely, different H_2O_2 concentrations might influence the relative role of ROS. To assess this effect, we examined the ROS concentrations and their contributions under five different H_2O_2 levels (0.5, 1, 3, 5, and 10 mM). The results are presented in Table S5. As shown in Table S5, increasing the H_2O_2 dosage leads to higher •OH concentrations and relative contributions, accompanied by a corresponding decrease in the contribution of triplet excited states ($^3C^*$). The measured •OH concentrations generally fall within a relatively narrow range under five different H_2O_2 concentration, with average values of (0.7–9.1) $\times 10^{-14}$ and (1.3–8.3) $\times 10^{-14}$ M, for coal and maize smoke WSOM, respectively. Specifically, we also noted that the $^1O_2$ contribution is only weakly affected by the H_2O_2 concentration. Given that this study mainly focuses on the role of •OH, all subsequent experiments were conducted at a relatively high H_2O_2 concentration. While additional experiments at varying H_2O_2 concentrations would provide valuable quantitative constraints on these processes, they are beyond the scope of the present study.

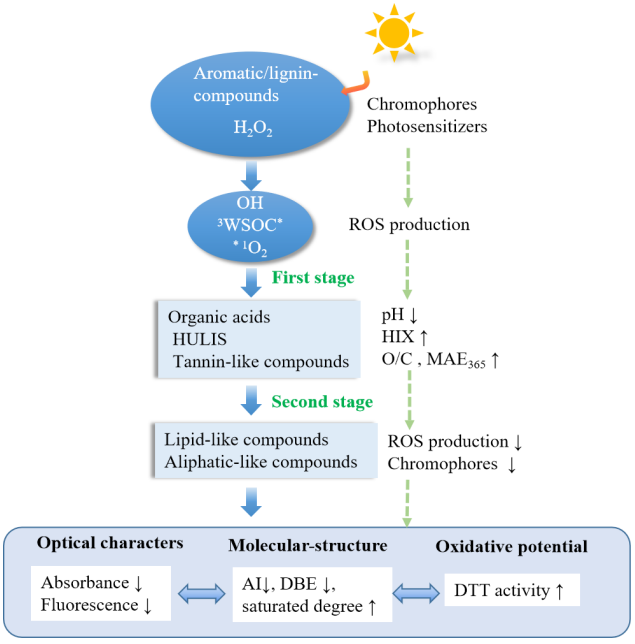

Figure 12. Proposed photochemical transformation pathways for two smoke extracts.

3.6.2 Photochemical transformation of smoke extracts

By introducing extra H_2O_2, the •OH concentration and its role in the photoaging of both smoke extracts were altered. The added •OH accounts for a major fraction of the total oxidants in both systems, thereby influencing the overall optical properties and chemical composition. Based on the ROS measurements and molecular analyses, a conceptual mechanism for the aqueous photooxidation of both smoke extracts is proposed (Fig. 12). Upon irradiation, photosensitizers in WSOM absorb photons and form triplet excited states ($^3PS^*$), which transfer energy or electrons to dissolved O_2, generating various ROS ($^1O_2$, $O_2^{\bullet-}$, $\cdot HO_2$, and •OH). These reactive species initiate and propagate oxidation processes, thereby modifying the chemical composition and optical properties of WSOM.

In the first stage, abundant •OH rapidly attacks electron-rich aromatic and conjugated structures, cleaving C = C and C–O bonds and causing a sharp decrease in WSOC and light absorbance. Meanwhile, both $^3Sen^*$ and $^1O_2$ selectively oxidizes lignin-like compounds, forming oxygenated intermediates such as carbonyls, and carboxylic acids, resulting in gradual decrease in solution pH (Fig. S7) and increase in O / C.

As the reaction proceeds, the depletion of aromatic chromophores suppresses further ROS formation, consistent with the observed decline in DTT activity. FT-ICR MS analysis further supports this evolution, revealing a shift from high H / C, low O / C aromatic compounds toward lipid- or aliphatic-like species.

Interestingly, although total WSOC decreased with aging, WSOC-normalized DTT activity increased due to probable highly DTT active species (e.g., quinone-like species). Similar trends have been observed in BBOA-WSOC OH-photooxidation aging, where oxidative potential decreased at the initial period (∼ 5 h) despite WSOC mass loss (Wong et al., 2019).

Overall, the aqueous photooxidation of two smoke extracts involves a dynamic interplay among •OH, $^3C^*$, and $^1O_2$. The early stage is dominated by •OH-driven degradation of chromophores, followed by secondary formation of oxygenated, potentially more toxic species through $^1O_2$ and triplet-state reactions. These processes jointly govern the chemical evolution, light-absorbing behavior, and oxidative potential of WSOM during photochemical aging.

Next, by integrating FT-ICR MS and ROS analyses, we further compared the molecular transformation mechanisms of the two types of smoke. Tables S6 and S7 list the top 10 most abundant compounds identified by FT-ICR MS before photolysis and after 11 and 23 h of irradiation, together with their DBE values, molecular formulas, inferred functional groups, and FT-ICR MS classifications.

Fresh coal-derived WSOM is mainly composed of CHO and CHOS compounds, including organosulfates (e.g., $C_{12}H_{26}O_4S$, $C_{17}H_{28}O_3S$, and $C_{18}H_{30}O_3S$), aromatic oxygenated species (e.g., $C_{12}H_{12}O_5$ and $C_{13}H_{14}O_5$), and aliphatic compounds (e.g., $C_{18}H_{36}O_3$). During photochemical processing, only limited transformation is observed among the top 10 compounds, although partial conversion of lignin-like structures into lipid-like species occurs.

Several molecular formulas (e.g., $C_{17}H_{28}O_3S$, $C_{18}H_{30}O_3S$, $C_{16}H_{32}O_2$, and $C_{18}H_{36}O_3$) persist before and after 11 h of irradiation, indicating their relative resistance to photochemical degradation. Consequently, the average molecular weight of coal-derived WSOM exhibits only minor variation during oxidation.

The transformation of coal smoke WSOM can be summarized by three main pathways. First, aromatic compounds (e.g., $C_{12}H_{12}O_5$ and $C_{13}H_{14}O_5$) undergo •OH-driven oxidation and tend to break down into smaller molecules, contributing to the loss of aromatic structures. Second, aliphatic compounds (e.g., $C_{18}H_{36}O_3$) are oxidized via •OH-initiated functionalization, forming more stable oxygenated fatty acid-like products such as $C_{16}H_{32}O_2$ and $C_{18}H_{36}O_2$, along with partially oxidized intermediates (e.g., $C_{18}H_{34}O_3$). Third, CHOS compounds exhibit partial stability, with long-chain organosulfates (e.g., $C_{18}H_{30}O_3S$) persisting throughout the oxidation process.

In contrast, maize smoke WSOM shows distinctly different behavior. The fresh sample was dominated by lignin-like compounds, such as $C_9H_{10}O_3$ and $C_9H_8O_3$, reflecting the prevalence of aromatic structures derived from biomass combustion. During aqueous-phase oxidation, these compounds undergo extensive transformation driven primarily by •OH attack, including hydrogen abstraction and electrophilic addition to aromatic rings. These reactions promote hydroxylation, denitration, and subsequent ring-opening processes, leading to the formation of highly oxygenated and lower-molecular-weight products. As a result, both aromaticity and average molecular weight decrease significantly. This trend is supported by the appearance of highly oxygenated species (e.g., $C_9H_{10}O_7$ and $C_9H_{18}O_6$ at 11 h), which shift toward higher O / C ratios in the Van Krevelen space. Meanwhile, lignin-like compounds are progressively transformed into lipid-like, tannin-like, and aliphatic species. Notably, the top 10 products at 11 and 23 h exhibit strong similarity (e.g., $C_{14}H_{22}O$, $C_{16}H_{32}O_2$, $C_{18}H_{36}O_2$, and $C_{12}H_{26}O_4S$), suggesting the formation of relatively stable oxidation products at later stages.

Overall, these results demonstrate that maize smoke undergoes more extensive oxidation, characterized by pronounced aromatic degradation and molecular fragmentation, whereas coal smoke exhibits higher chemical stability, with limited molecular transformation and a greater persistence of initial compounds.

4 Conclusions

This study systematically investigated the aqueous-phase •OH-driven photodegradation of coal and maize smoke extracts, providing molecular-level insights into their molecular and optical evolution. EEM-PARAFAC resolved one humic-like and two protein-like components, revealing distinct temporal patterns between coal and maize systems. FT-ICR MS further showed that both samples were dominated by CHO and CHON compounds, with maize smoke enriched in CHON species and coal smoke containing a higher fraction of sulfur-containing compounds.

Aqueous photooxidation led to increased molecular saturation and reduced aromaticity, as evidenced by declining DBE and AI values. Lignin-like compounds were progressively depleted, accompanied by an increase in lipid- and aliphatic-like species, suggesting the breakdown of conjugated structures and the formation of more saturated, oxygenated products. These transformations reduced chromophoric content through double-bond cleavage and aromatic ring opening, resulting in decreased light absorption and fluorescence.

The contributions of ROS to photodegradation followed the order $\bullet OH > {}^3C^* > {}^1O_2$, highlighting the dominant role of •OH in aqueous-phase processing. Despite these common trends, distinct photochemical pathways were observed. Maize-derived WSOM exhibited more rapid oxidation during the early stage, likely driven by OH-functionalization reactions, whereas coal-derived WSOM showed greater compositional stability. Mechanistically, ROS promoted the conversion of lignin-like aromatics into highly oxygenated products via hydroxylation and ring-opening, while lipid-like compounds undergo functionalization and fragmentation. Secondary reactions with sulfate lead to the formation of organosulfates.

HR-AMS results confirmed the formation of low-molecular-weight carboxylic acids (e.g., oxalate), accompanied by decreasing pH and increasing oxidation state of aqSOA, particularly in maize systems. Although total WSOC decreased during photodegradation, the WSOC-normalized oxidative potential increased, as indicated by enhanced DTT consumption, likely due to the formation of nitrogen-containing compounds in coal smoke and reactive quinones in maize smoke. Furthermore, maize-derived aqSOA exhibited higher oxidation levels, whereas coal smoke produced higher aqSOA mass yields.

Overall, aqueous-phase photochemical processing simultaneously weakens optical properties and enhances chemical reactivity. From an atmospheric perspective, cloud and fog processing can substantially modify the properties of smoke-derived WSOM. The transformation of aromatic chromophores into more saturated products reduces brown carbon light absorption, potentially weakening its direct radiative forcing. At the same time, the formation of highly oxidized and redox-active species may enhance aerosol oxidative potential and toxicity. These findings underscore the importance of incorporating aqueous-phase transformations into atmospheric models to more accurately assess the climate and air quality impacts of emissions from different fuel sources.

Data availability. All data used in this study are available upon request.

Supplement. The supplement related to this article is available online at https://doi.org/10.5194/acp-26-8255-2026-supplement.

Author contributions. ZY and XG developed the research objectives and designed the experiments. DH and XH set up the combustion sampling apparatus and collected samples. DH and QC conducted the photochemistry experiments and analyzed the data with the help of XH. ZY prepared the manuscript with contributions from all co-authors. ZY and XG provided supervision and guidance during the experiments and writing.

Competing interests. The contact author has declared that none of the authors has any competing interests.

Disclaimer. Publisher's note: Copernicus Publications remains neutral with regard to jurisdictional claims made in the text, published maps, institutional affiliations, or any other geographical representation in this paper. The authors bear the ultimate responsibility for providing appropriate place names. Views expressed in the text are those of the authors and do not necessarily reflect the views of the publisher.

Acknowledgements. We appreciate the comments and efforts of the two anonymous reviewers.

Financial support. The authors acknowledge support from the Natural Science Foundation of Jiangsu Province (grant no. BK20221405) and the National foreign expert project (grant no. H20240368). We are also thankful for funding support from the Natural Science Foundation of China (grant no. 22361162668), the Natural Science Foundation of the Jiangsu Higher Education Institutions of China (grant no. 25KJD170010), and the Postgraduate Research & Practice Innovation Program of Jiangsu Province (grant no. SJCX24_1808).

Review statement. This paper was edited by Dantong Liu and reviewed by two anonymous referees.

References

Arakaki, T., Anastasio, C., Kuroki, Y., Nakajima, H., Okada, K., Kotani, Y., Handa, D., Azechi, S., Kimura, T., Tsuhako, A., and Miyagi, Y.: A general scavenging rate constant for reaction of hydroxyl radical with organic carbon in atmospheric waters, Environ. Sci. Technol., 47, 8196–8203, https://doi.org/10.1021/es401927b, 2013.

Arciva, S., Niedek, C., Mavis, C., Yoon, M., Sanchez, M. E., Zhang, Q., and Anastasio, C.: Aqueous •OH oxidation of highly substituted phenols as a source of secondary organic aerosol, Environ. Sci. Technol., 56, 9959–9967, https://doi.org/10.1021/acs.est.2c02225, 2022.

Arciva, S., Ma, L., Mavis, C., Guzman, C., and Anastasio, C.: Formation and loss of light absorbance by phenolic aqueous SOA by •OH and an organic triplet excited state, Atmos. Chem. Phys., 24, 4473–4485, https://doi.org/10.5194/acp-24-4473-2024, 2024.

Bogler, S., Daellenbach, K. R., Bell, D. M., Prévôt, A. S. H., El Haddad, I., and Borduas-Dedekind, N.: Singlet oxygen seasonality in aqueous PM_{10} is driven by biomass burning and anthropogenic secondary organic aerosol, Environ. Sci. Technol., 56, 15389–15397, https://doi.org/10.1021/acs.est.2c04554, 2022.

Cao, T., Xu, C., Chen, H., Song, J., Li, J., Song, H., Jiang, B., Zhong, Y., and Peng, P.: Molecular insight into aqueous-phase photolysis and photooxidation of water-soluble organic matter emitted from biomass burning and coal combustion, Atmos. Chem. Phys., 25, 11597–11610, https://doi.org/10.5194/acp-25-11597-2025, 2025.

Chen, Q., Wang, M., Wang, Y., Zhang, L., Li, Y., and Han, Y.: Oxidative potential of water-soluble matter associated with chromophoric substances in $PM_{2.5}$ over Xi'an, China, Environ. Sci. Technol., 53, 8574–8584, https://doi.org/10.1021/acs.est.9b01976, 2019.

Chen, W., Zhang, H., Xu, S., Jia, H., Qi, Z., Farooq, U., Wang, Z., and Dai, Q.: New insights into the molecular characteristics-dependent light absorption variation of water-soluble organic matter in biomass burning smoke, Atmos. Res., 316, 107951, https://doi.org/10.1016/j.atmosres.2025.107951, 2025.

Cook, R. D., Lin, Y.-H., Peng, Z., Boone, E., Chu, R. K., Dukett, J. E., Gunsch, M. J., Zhang, W., Tolic, N., Laskin, A., and Pratt, K. A.: Biogenic, urban, and wildfire influences on the molecular composition of dissolved organic compounds in cloud water, Atmos. Chem. Phys., 17, 15167–15180, https://doi.org/10.5194/acp-17-15167-2017, 2017.

Fan, X., Wei, S., Zhu, M., Song, J., and Peng, P.: Comprehensive characterization of humic-like substances in smoke PM2.5 emitted from the combustion of biomass materials and fossil fuels, Atmos. Chem. Phys., 16, 13321–13340, https://doi.org/10.5194/acp-16-13321-2016, 2016.

Fan, X., Li, M., Cao, T., Cheng, C., Li, F., Xie, Y., Wei, S., Song, J., and Peng, P.: Optical properties and oxidative potential of water- and alkaline-soluble brown carbon in smoke particles emitted from laboratory simulated biomass burning, Atmos. Environ., 194, 48–57, https://doi.org/10.1016/j.atmosenv.2018.09.025, 2018.

Fan, X., Xie, S., Yu, X., Cheng, A., Chen, D., Ji, W., Liu, X., Song, J., and Peng, P.: Molecular-level transformations of biomass burning-derived water-soluble organic carbon during dark aqueous OH oxidation: Insights from absorption, fluorescence, high-performance size exclusion chromatography and high-resolution mass spectrometry analysis, Sci. Total Environ., 912, 169290, https://doi.org/10.1016/j.scitotenv.2023.169290, 2024.

Fang, Z., Lai, A., Cai, D., Li, C., Carmieli, R., Chen, J., Wang, X., and Rudich, Y.: Secondary organic aerosol generated from biomass burning emitted phenolic compounds: Oxidative potential, reactive oxygen species,

and cytotoxicity, Environ. Sci. Technol., 58, 8194–8206, https://doi.org/10.1021/acs.est.3c09903, 2024.

Gerritz, L., Wei, J., Fang, T., Wong, C., Klodt, A. L., Nizkorodov, S. A., and Shiraiwa, M.: Reactive oxygen species formation and peroxide and carbonyl decomposition in aqueous photolysis of secondary organic aerosols, Environ. Sci. Technol., 58, 4716–4726, https://doi.org/10.1021/acs.est.3c08662, 2024.

Go, B. R., Li, Y. J., Huang, D. D., Wang, Y., and Chan, C. K.: Comparison of aqueous secondary organic aerosol (aqSOA) product distributions from guaiacol oxidation by non-phenolic and phenolic methoxybenzaldehydes as photosensitizers in the absence and presence of ammonium nitrate, Atmos. Chem. Phys., 23, 2859–2875, https://doi.org/10.5194/acp-23-2859-2023, 2023.

Go, B. R., Li, Y. J., Huang, D. D., and Chan, C. K.: Aqueous-phase photoreactions of mixed aromatic carbonyl photosensitizers yield more oxygenated, oxidized, and less light-absorbing secondary organic aerosol (SOA) than single systems, Environ. Sci. Technol., 58, 7924–7936, https://doi.org/10.1021/acs.est.3c10199, 2024.

Hems, R. F., Schnitzler, E. G., Bastawrous, M., Soong, R., Simpson, A. J., and Abbatt, J. P. D.: Aqueous photoreactions of wood smoke brown carbon, ACS Earth Space Chem., 4, 1149–1160, https://doi.org/10.1021/acsearthspacechem.0c00117, 2020.

Hu, D., Ye, Z., Wang, Z., Topping, D., Aruffo, E., Wang, H., and Ge, X.: Kinetics and quantum yield of photosensitized reactions from substituted phenols via chemical probe approach, Atmos. Environ., 360, 121419, https://doi.org/10.1016/j.atmosenv.2025.121419, 2025a.

Hu, D., Wang, Z., Aruffo, E., Dai, X., Zhao, Z., and Ye, Z.: Kinetics of different substituted Phenolic compounds' aqueous OH oxidation in atmosphere, Atmosphere, 16, https://doi.org/10.3390/atmos16050567, 2025b.

Huang, Y., Li, X., Huang, D. D., Lei, R., Zhou, B., Zhang, Y., and Ge, X.: Machine-learning-assisted chemical characterization and optical properties of atmospheric brown carbon in Nanjing, China, Atmos. Chem. Phys., 25, 7619–7645, https://doi.org/10.5194/acp-25-7619-2025, 2025.

Jiang, H. and Jang, M.: Dynamic oxidative potential of atmospheric organic aerosol under ambient sunlight, Environ. Sci. Technol., 52, 7496–7504, https://doi.org/10.1021/acs.est.8b00148, 2018.

Jiang, W., Misovich, M. V., Hettiyadura, A. P. S., Laskin, A., McFall, A. S., Anastasio, C., and Zhang, Q.: Photosensitized reactions of a phenolic carbonyl from wood combustion in the aqueous phase – Chemical evolution and light absorption properties of aqSOA, Environ. Sci. Technol., https://doi.org/10.1021/acs.est.0c07581, 2021.

Jiang, W., Niedek, C., Anastasio, C., and Zhang, Q.: Photoaging of phenolic secondary organic aerosol in the aqueous phase: evolution of chemical and optical properties and effects of oxidants, Atmos. Chem. Phys., 23, 7103–7120, https://doi.org/10.5194/acp-23-7103-2023, 2023.

Lei, R., Sha, Y., Meng, H., Huang, Y., Ye, J., Huang, D. D., Zhang, Y., Wu, Y., Li, Y., and Ge, X.: Aqueous phase photolysis of 4-nitrocatechol: Reaction kinetics, evolutions of chemical composition, light absorption and oxidation potential, Atmos. Environ., 343, 120981, https://doi.org/10.1016/j.atmosenv.2024.120981, 2025.

Lei, Y., Yu, Y., Lei, X., Liang, X., Cheng, S., Ouyang, G., and Yang, X.: Assessing the use of probes and quenchers for understanding the reactive species in advanced oxidation processes, Environ. Sci. Technol., 57, 5433–5444, https://doi.org/10.1021/acs.est.2c09338, 2023.

Lei, Y., Lei, X., Tian, G., Yang, J., Huang, D., Yang, X., Chen, C., and Zhao, J.: Optical variation and molecular transformation of brown carbon during oxidation by NO_3• in the aqueous phase, Environ. Sci. Technol., 58, 3353–3362, https://doi.org/10.1021/acs.est.3c08726, 2024.

Leresche, F., Salazar, J. R., Pfotenhauer, D. J., Hannigan, M. P., Majestic, B. J., and Rosario-Ortiz, F. L.: Photochemical aging of atmospheric particulate matter in the aqueous phase, Environ. Sci. Technol., 55, 13152–13163, https://doi.org/10.1021/acs.est.1c00978, 2021.

Li, F., Tsona, N. T., Li, J., and Du, L.: Aqueous-phase oxidation of syringic acid emitted from biomass burning: Formation of light-absorbing compounds, Sci. Total Environ., 765, 144239, https://doi.org/10.1016/j.scitotenv.2020.144239, 2021.

Li, F., Zhou, S., Du, L., Zhao, J., Hang, J., and Wang, X.: Aqueous-phase chemistry of atmospheric phenolic compounds: A critical review of laboratory studies, Sci. Total Environ., 856, 158895, https://doi.org/10.1016/j.scitotenv.2022.158895, 2023.

Li, F., Zhou, S., Zhao, J., Hang, J., Lu, H., Li, X., Gao, M., Li, Y., and Wang, X.: Aqueous photosensitization of syringaldehyde: Reactivity, effects of environmental factors, and formation of brown carbon products, ACS Earth Space Chem., 8, 1193–1203, https://doi.org/10.1021/acsearthspacechem.4c00004, 2024a.

Li, L., Han, Y., Li, J., Lin, Y., Zhang, X., Wang, Q., and Cao, J.: Effects of photochemical aging on the molecular composition of organic aerosols derived from agricultural biomass burning in whole combustion process, Sci. Total Environ., 946, 174152, https://doi.org/10.1016/j.scitotenv.2024.174152, 2024b.

Lin, P., Aiona, P. K., Li, Y., Shiraiwa, M., Laskin, J., Nizkorodov, S. A., and Laskin, A: Molecular characterization of brown carbon in biomass burning aerosol particles, Environ. Sci. Technol., 50, 11815–11824, https://https://doi.org/10.1021/acs.est.6b03024, 2016.

Li, X., Tao, Y., Zhu, L., Ma, S., Luo, S., Zhao, Z., Sun, N., Ge, X., and Ye, Z.: Optical and chemical properties and oxidative potential of aqueous-phase products from OH and $^3C^*$-initiated photooxidation of eugenol, Atmos. Chem. Phys., 22, 7793–7814, https://doi.org/10.5194/acp-22-7793-2022, 2022.

Liu-Kang, C., Sokolova, A., Gong, Y., Fahy, W. D., Peng, H., and Abbatt, J. P. D.: Light exposure of wood smoke aerosol: Connecting optical properties, oxidation, radical formation, and chemical composition, ACS EST Air, 1, 273–282, https://doi.org/10.1021/acsestair.3c00063, 2024.

Ma, L., Worland, R., Jiang, W., Niedek, C., Guzman, C., Bein, K. J., Zhang, Q., and Anastasio, C.: Predicting photooxidant concentrations in aerosol liquid water based on laboratory extracts of ambient particles, Atmos. Chem. Phys., 23, 8805–8821, https://doi.org/10.5194/acp-23-8805-2023, 2023.

Ma, L., Worland, R., Heinlein, L., Guzman, C., Jiang, W., Niedek, C., Bein, K. J., Zhang, Q., and Anastasio, C.: Seasonal variations in photooxidant formation and light absorption in aqueous extracts of ambient particles, Atmos. Chem. Phys., 24, 1–21, https://doi.org/10.5194/acp-24-1-2024, 2024.

Mahamuni, G., Rutherford, J., Davis, J., Molnar, E., Posner, J. D., Seto, E., Korshin, G., and Novosselov, I.: Excitation–emission matrix spectroscopy for analysis of chemical composition of

combustion generated particulate matter, Environ. Sci. Technol., 54, 8198–8209, https://doi.org/10.1021/acs.est.0c01110, 2020.

Manfrin, A., Nizkorodov, S. A., Malecha, K. T., Getzinger, G. J., McNeill, K., and Borduas-Dedekind, N.: Reactive oxygen species production from secondary organic aerosols: The importance of singlet oxygen, Environ. Sci. Technol., 53, 8553–8562, https://doi.org/10.1021/acs.est.9b01609, 2019.

Ning, C., Tang, Y., Sun, S., Wang, D., and Gao, Y.: Molecular level characteristics and sources of rainwater water-soluble organic matter in different regions of China by FT-ICR MS, Atmos. Environ., 350, 121175, https://doi.org/10.1016/j.atmosenv.2025.121175, 2025.

Song, J., Li, M., Jiang, B., Wei, S., Fan, X., and Peng, P.: Molecular characterization of water-soluble humic like substances in smoke particles emitted from combustion of biomass materials and coal using ultrahigh-resolution electrospray ionization Fourier Transform Ion Cyclotron Resonance Mass Spectrometry, Environ. Sci. Technol., 52, 2575–2585, https://doi.org/10.1021/acs.est.7b06126, 2018.

Tang, J., Li, J., Su, T., Han, Y., Mo, Y., Jiang, H., Cui, M., Jiang, B., Chen, Y., Tang, J., Song, J., Peng, P., and Zhang, G.: Molecular compositions and optical properties of dissolved brown carbon in biomass burning, coal combustion, and vehicle emission aerosols illuminated by excitation–emission matrix spectroscopy and Fourier transform ion cyclotron resonance mass spectrometry analysis, Atmos. Chem. Phys., 20, 2513–2532, https://doi.org/10.5194/acp-20-2513-2020, 2020.

Tang, R., Ma, J., Zhang, R., Cui, W., Qin, Y., Chu, Y., Qin, Y., Vogel, A. L., and Chan, C. K.: Enhanced sulfate formation in mixed biomass burning and sea-salt interactions mediated by photosensitization: effects of chloride, nitrogen-containing compounds, and atmospheric aging, Atmos. Chem. Phys., 25, 425–439, https://doi.org/10.5194/acp-25-425-2025, 2025.

Tomaz, S., Cui, T., Chen, Y., Sexton, K. G., Roberts, J. M., Warneke, C., Yokelson, R. J., Surratt, J. D., and Turpin, B. J.: Photochemical cloud processing of primary wildfire emissions as a potential source of secondary organic aerosol, Environ. Sci. Technol., 52, 11027–11037, https://doi.org/10.1021/acs.est.8b03293, 2018.

Verma, V., Rico-Martinez, R., Kotra, N., King, L., Liu, J., Snell, T. W., and Weber, R. J.: Contribution of water-soluble and insoluble components and their hydrophobic/hydrophilic subfractions to the reactive oxygen species-generating potential of fine ambient aerosols, Environ. Sci. Technol., 46, 11384–11392, https://doi.org/10.1021/es302484r, 2012.

Vione, D., Albinet, A., Barsotti, F., Mekic, M., Jiang, B., Minero, C., Brigante, M., and Gligorovski, S.: Formation of substances with humic-like fluorescence properties, upon photoinduced oligomerization of typical phenolic compounds emitted by biomass burning, Atmos. Environ., 206, 197–207, https://doi.org/10.1016/j.atmosenv.2019.03.005, 2019.

Wang, H., Zheng, N., Du, H., Chen, Z., Sha, H., Zhou, H., and Ye, Z.: Microheterogeneous photogeneration of hydroxyl radical in sunlit dissolved black carbon solution, J. Hazard. Mater., 498, 139840, https://doi.org/10.1016/j.jhazmat.2025.139840, 2025.

Wang, J. and Wang, S: Reactive species in advanced oxidation processes: Formation, identification and reaction mechanism, Chem. Eng. J., 401, 126158, https://doi.org/10.1016/j.cej.2020.126158, 2020.1261582020, 2020.

Wang, X., Hayeck, N., Brüggemann, M., Yao, L., Chen, H., Zhang, C., Emmelin, C., Chen, J., George, C., and Wang, L.: Chemical characteristics of organic aerosols in Shanghai: A study by ultrahigh-performance liquid chromatography coupled with orbitrap mass spectrometry, J. Geophys. Res. Atmos., 122, 11703–11722, https://doi.org/10.1002/2017JD026930, 2017.

Wong, J. P. S., Nenes, A., and Weber, R. J.: Changes in light absorptivity of molecular weight separated brown carbon due to photolytic aging, Environ. Sci. Technol., 51, 8414–8421, https://doi.org/10.1021/acs.est.7b01739, 2017.

Wong, J. P. S., Tsagkaraki, M., Tsiodra, I., Mihalopoulos, N., Violaki, K., Kanakidou, M., Sciare, J., Nenes, A., and Weber, R. J.: Effects of atmospheric processing on the oxidative potential of biomass burning organic aerosols, Environ. Sci. Technol., 53, 6747–6756, https://doi.org/10.1021/acs.est.9b01034, 2019.

Wu, G., Fu, P., Ram, K., Song, J., Chen, Q., Kawamura, K., Wan, X., Kang, S., Wang, X., Laskin, A., and Cong, Z.: Fluorescence characteristics of water-soluble organic carbon in atmospheric aerosol, Environ. Pollut., 268, 115906, https://doi.org/10.1016/j.envpol.2020.115906, 2021.

Yang, N., Wang, J., Jacob, D. J., Ye, J., Sheng, M., Niu, M., Qin, Y., Ge, X., Sun, Y., Wang, Z., Wang, Y., Wu, F., Liu, C.-Q., George, C., and Fu, P.: Aqueous production of sulfur-containing aerosols from nitroaromatic compounds and SO_2 in wintertime urban haze, Sci. Bull., 70, 1846–1855, https://doi.org/10.1016/j.scib.2025.03.013, 2025.

Ye, Z., Hu, D., Wang, Z., Wang, H., and Ge, X.: Aqueous photochemical aging of water-soluble smoke particles from crop straws burning, Atmos. Environ., 340, 120897, https://doi.org/10.1016/j.atmosenv.2024.120897, 2025.

Zhang, H., Wu, L., Qian, W., Ni, J., Wei, R., Qi, Z., and Chen, W.: Spectral characteristics of dissolved organic carbon derived from biomass-pyrogenic smoke (SDOC) in the aqueous environment and its solubilization effect on hydrophobic organic pollutants, Water Res., 203, 117515, https://doi.org/10.1016/j.watres.2021.117515, 2021.

Zhang, J., Shrivastava, M., Ma, L., Jiang, W., Anastasio, C., Zhang, Q., and Zelenyuk, A.: Modeling novel aqueous particle and cloud chemistry processes of biomass burning phenols and their potential to form secondary organic aerosols, Environ. Sci. Technol., 58, 3776–3786, https://doi.org/10.1021/acs.est.3c07762, 2024.